

CT Protocols for Attenuation Correction and Segmentation in ^{99m}Tc -MAA SPECT/CT for ^{90}Y Radioembolization Treatment Planning – a Simulation Study

Zhonglin Lu

University of Macau

Greta S. P. Mok (✉ gretamok@um.edu.mo)

University of Macau <https://orcid.org/0000-0002-2962-2087>

Original research

Keywords: ^{90}Y radioembolization, ^{99m}Tc -macroaggregated albumin, SPECT/CT, attenuation correction, segmentation, lung shunt fraction, tumor-to-normal liver ratio, injected activity, partition model

Posted Date: May 28th, 2020

DOI: <https://doi.org/10.21203/rs.3.rs-31563/v1>

License: © ⓘ This work is licensed under a Creative Commons Attribution 4.0 International License.

[Read Full License](#)

1 **CT Protocols for Attenuation Correction and Segmentation in**
2 **^{99m}Tc -MAA SPECT/CT for ^{90}Y Radioembolization Treatment**
3 **Planning – a Simulation Study**

4

5 Zhonglin Lu¹ and Greta S. P. Mok^{1,2*}

6 ¹ Biomedical Imaging Laboratory (BIG), Department of Electrical and Computer Engineering, Faculty of Science
7 and Technology & ² Center for Cognitive and Brain Sciences, Institute of Collaborative Innovation, University of
8 Macau, Avenida da Universidade, Taipa, Macau SAR, China

9

10 * Correspondence: gretamok@um.edu.mo.

11

12

13

14

15

16

17

18

19

20

21

22

23

24

25

26 **Abstract**

27 **Background:** Conventional ^{99m}Tc -macroaggregated albumin (^{99m}Tc -MAA) planar scintigraphy
28 overestimates lung shunt fraction (LSF) as compared to SPECT/CT in ^{90}Y radioembolization
29 treatment planning. However, the respiratory motion artifact due to the temporal mismatch
30 between static SPECT and helical CT (HCT) may compromise the SPECT quantitation accuracy
31 by incorrect attenuation correction (AC) and volume-of-interest segmentation. The goal of this
32 study is to systematically assess different AC and segmentation protocols for LSF, tumor-to-
33 normal liver (TNR), organ absorbed dose and injected activity (IA) estimation in ^{99m}Tc -MAA
34 SPECT/CT.

35 **Methods:** The 4D XCAT phantom was used to simulate 10 patient anatomies with ^{99m}Tc -MAA
36 distribution based on the clinical data, each with LSF of 5%, 10%, 15% and 20%, axial
37 respiratory motion of 2 cm, different TNR and tumor size. An analytical projector for low energy
38 high resolution parallel-hole collimator was used to simulate realistic noisy planar acquisitions,
39 and 128 projections over 360° for SPECT, both modeling attenuation, scatter and geometric
40 collimator-detector-response. Five attenuation maps, i.e., (i) HCT at end-inspiration (HCT-IN),
41 (ii) HCT at mid-respiration (HCT-MID), (iii) HCT at end-expiration (HCT-EX), (iv) cine
42 averaged CT (CACT) and (v) interpolated average CT (IACT) were applied for SPECT AC and
43 segmentation in LSF, dosimetric and IA evaluation. Mid-respiratory phases were also extracted
44 from CACT/IACT for VOI segmentation while CACT/IACT were used for AC, i.e., hybrid CT
45 protocols.

46 **Results:** For LSF estimation, SPECT/CACT has the least absolute errors. Planar significantly
47 overestimates LSF and lung absorbed dose compared to SPECT especially for LSF of 5%.
48 SPECT-based is better than CT-based segmentation in TNR estimation. There is no statistically

49 significant difference for different CT protocols for TNR, normal liver and tumor absorbed dose
50 estimation. Hybrid CTs and HCT-MID performed the best for IA especially for higher LSF.

51 **Conclusions:** ^{99m}Tc -MAA SPECT/CT with an appropriate choice of CT protocol for AC and
52 segmentation is superior to planar in LSF and lung absorbed dose estimation. The 4D CT
53 protocols are recommended for AC and segmentation to alleviate respiratory artifacts and
54 improve quantitation accuracy in ^{90}Y radioembolization treatment planning. HCT-EX would also
55 be a recommended choice if 4D CT is not available.

56

57 **Keywords:** ^{90}Y radioembolization; ^{99m}Tc -macroaggregated albumin; SPECT/CT; attenuation
58 correction; segmentation; lung shunt fraction; tumor-to-normal liver ratio; injected activity;
59 partition model.

60

61

62

63

64

65

66

67 **Background**

68 ^{90}Y radioembolization, also known as selective internal radiation therapy (SIRT) is increasingly
69 adopted as an efficient treatment for patients with inoperable hepatocellular carcinoma (HCC)
70 and liver metastasis, using microspheres loaded with radioactive isotope ^{90}Y whose primary β^-
71 emission energy is 2.28 MeV [1]. Two types of commercial ^{90}Y microspheres are currently
72 available: resin microspheres (SIR-Sphere®, Sirtex, Medical, Sydney, Australia) and glass
73 microspheres (TheraSphere®, BTG, Boston Scientific, Massachusetts, United States). These
74 microspheres are injected through a catheter connecting to the hepatic artery which mainly
75 supplies the tumor while portal vein feeds the normal liver parenchyma, resulting in high
76 radiation dose to tumor when sparing normal liver [2]. Complications of ^{90}Y radioembolization
77 are mainly radiation-induced liver disease, radiation pneumonitis, gastrointestinal ulceration and
78 diarrhea [3]. Thus, prior to ^{90}Y microspheres treatment, appropriate imaging evaluation should
79 be performed to determine parameters related to complications such as lung shunting fraction
80 (LSF), tumor-to-normal liver ratio (TNR) and injected activity (IA) based on the partition model
81 [4]. Radionuclide imaging is a prevailing method to investigate these parameters, using $^{99\text{m}}\text{Tc}$ -
82 macroaggregated albumin ($^{99\text{m}}\text{Tc}$ -MAA) as a surrogate for ^{90}Y microsphere [5].

83 Conventional $^{99\text{m}}\text{Tc}$ -MAA planar imaging is limited in lungs and liver delineation due to
84 organs overlap and lack of anatomical references. Additionally, planar images suffer from poor
85 image quality due to the limited compensations available. Therefore, previous studies reported
86 that the LSF was over estimated using planar scintigraphy as compared to quantitative $^{99\text{m}}\text{Tc}$ -
87 MAA SPECT/CT [6-8]. In addition, TNR, tumor and normal liver volume can be measured on
88 SPECT/CT or contrast CT for ^{90}Y treatment planning [5].

89 Nonetheless, the mismatch between the sequential SPECT and conventional helical CT (HCT)

90 acquisitions leads to the respiratory artifacts on SPECT reconstructed images especially near the
91 diaphragmatic region of the lower lungs and upper liver [9, 10], mainly due to the improper
92 attenuation correction (AC) [11, 12]. That would potentially degrade the ^{99m}Tc -MAA SPECT/CT
93 quantitative accuracy, affecting the LSF and TNR calculation. The use of average CT, including
94 cine average CT (CACT) and our previously proposed interpolated average CT (IACT), has been
95 proven to be an effective AC method to reduce the respiratory artifacts and improve the
96 quantification for thoracic SPECT [11] and PET [13-15]. Besides, segmentation of lungs, liver
97 and tumors also highly affects the dosimetric accuracy for ^{99m}Tc -MAA SPECT/CT [16]. To the
98 best of our knowledge, the optimal CT protocol has not yet been determined for ^{99m}Tc -MAA
99 SPECT/CT. This study aims to evaluate the use of different CT protocols, including HCTs
100 acquired at end-inspiration (HCT-IN), end-expiration (HCT-EX), mid-respiration (HCT-MID),
101 CACT and IACT as AC maps and segmentation references for ^{99m}Tc -MAA SPECT/CT based on
102 simulations with known truth. The LSF and lung absorbed dose measured from the planar
103 scintigraphy were also shown references.

104

105 **Materials and Methods**

106 **Phantom population**

107 The 4D digital extended cardiac torso (XCAT) phantom [17] was employed in this study to
108 model 10 different patient anatomies varying in gender, body size and heart size [18] as well as
109 TNR (4 to 11.4), spherical tumor size (2 cm to 8.7 cm in diameter) and location (Table 1) based
110 on the clinical data with ^{99m}Tc -MAA distribution (Table 2) [19]. In addition, each patient
111 anatomy was modeled with four different LSFs, i.e., 5%, 10%, 15% and 20% (Fig. 1). Axial

112 respiratory motion of 2 cm and anterior-posterior expansion of 1.2 cm with a period of 4.8 s
 113 divided into 24 frames was modeled for the respiratory cycle. The average activity map of 24
 114 frames and the corresponding averaged attenuation map at 140 keV were generated. For the
 115 purpose of modeling the continuous nature of the activity distribution, XCAT phantoms with a
 116 voxel size of 0.221 cm were collapsed to a bin size of 0.442 cm.

117

118 Table 1. Anatomy of XCAT phantoms

	Lung volume (ml)	Normal liver volume (ml)	Tumor volume (ml)	TNR
Phantom #1	3403	1855	17	11.4
Phantom #2	4917	1996	346	6
Phantom #3, #4*	2564	1084	48	8.2
Phantom #5	3622	1624	6	7
Phantom #6	3403	1855	17	7
Phantom #7	3403	1747	125	11.4
Phantom #8	2446	929	125	5.2
Phantom #9	3530	1555	74	4
Phantom #10	4876	2269	66/23	9

119 *Phantom #3 and Phantom #4 have different tumor locations.

120

121

122

123

124

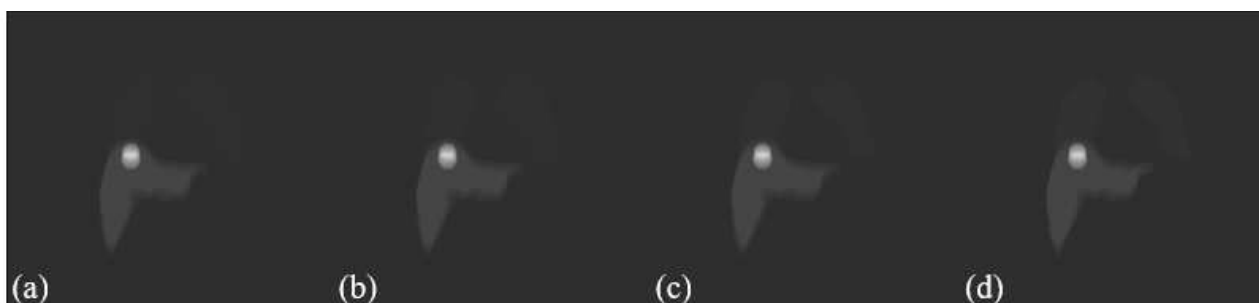
125

126

127 Table 2. ^{99m}Tc-MAA distribution of XCAT phantoms

Unit: Counts/voxel	Lungs				Normal liver	Tumor
	5% LSF	10% LSF	15% LSF	20% LSF		
Phantom #1	22	47	75	106	700	8000
Phantom #2	30	64	102	145		4200
Phantom #3, #4	21	45	71	101		5740
Phantom #5	17	36	57	80		4900
Phantom #6	21	45	72	102		4900
Phantom #7	34	73	115	164		8000
Phantom #8	24	50	80	113		3640
Phantom #9	19	41	65	92		2800
Phantom #10	23	49	78	110		6300

128



129

130 FIG .1. Phantom #6 with LSF of (a) 5%, (b) 10%, (c) 15% and (d) 20%.

131

132 **Simulation study**

133 We simulated a standard clinical dual head SPECT/CT system with a crystal thickness of 2.54

134 cm mounted with a low energy high resolution (LEHR) parallel-hole collimator using an

135 analytical projector [20]. For the planar protocol, anterior and posterior planar images were

136 generated in a supine position for 5 min/view, covering both lungs and the liver. For the

137 SPECT/CT protocol, 128 projections were generated over 360° with 30 s/view, using 20%

138 energy window centered at the photopeak of 140 keV. Both protocols modeled attenuation,

139 scatter and collimator-detector response (CDR). The scatter modeling (for SPECT and planar)
140 and correction (for SPECT only) were achieved by the effective source scatter estimation method
141 [21]. The Poisson noise was modelled in the SPECT projections and planar images (Fig. 2) based
142 on the normalized standard deviation (NSD) of a relatively uniform region-of-interest (ROI)
143 drawn in the liver region of the clinical SPECT projection data and planar data, respectively. For
144 the clinical count level reference, the injected ^{99m}Tc -MAA activity was 111 MBq. The one bed
145 position (axial field of view of 40 cm) SPECT acquisition time was 25 s/projection for 60
146 projections, while the planar acquisition was also with one bed position (covering chest to liver)
147 and 1000 kcts were collected. There was no AC or scatter correction (SC) performed in planar
148 images [22]. The average attenuation maps as well as the attenuation maps of the XCAT
149 phantoms in end-inspiration, middle-respiration and end-expiration phases were used to generate
150 CT projections by an analytical projector and then added with Gaussian noise whose level was
151 determined based on the clinical CT data [23]. The noisy projections were then reconstructed
152 using a filtered back-projection algorithm to obtain corresponding noisy CACT, HCT-IN, HCT-
153 MID and HCT-EX (Fig. 3a-d). The HCT-IN and HCT-EX were applied to generate IACT (Fig.
154 3e) via image registration and interpolation based on the standard XCAT respiratory curve [23,
155 24]. Additionally, another set of contrast HCT-IN, HCT-MID and HCT-EX with enhanced tumor
156 intensity was modeled.

157 Ordered subset expectation maximization (OS-EM) with 4 iterations and 16 subsets, i.e., a
158 total of 64 updates, was used for image reconstruction with AC, SC and CDR modelling during
159 the reconstruction. Different CT attenuation maps were used for AC in reconstruction
160 respectively.

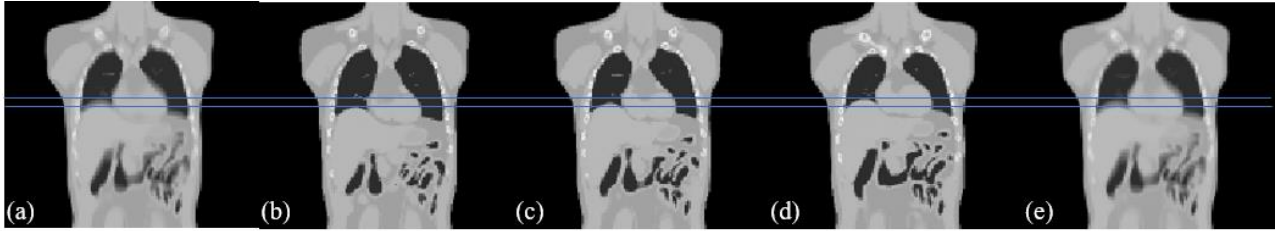


161

162

FIG. 2. Noisy anterior (left) and posterior (right) planar images of Phantom #3.

163



164

165

FIG. 3. (a) CACT, (b) HCT-IN, (c) HCT-MID, (d) HCT-EX and (e) IACT of Phantom #1. Blue

166

lines represent motion range of 2 cm.

167

168 Data analysis

169 *LSF estimation*

170

For planar images, ROIs of the lungs and livers were manually delineated on anterior and

171

posterior views. Left and right lungs were segmented out together and there was a gap of about 1

172

cm between the liver and lung interface (Fig. 4) [8]. In this study, the geometric mean (GM) was

173

measured for the lungs and liver using the following equation.

174

$$GM = \sqrt{C_A \times C_P} \quad (1)$$

175

where C_A and C_P are the total counts in the ROIs on anterior and posterior views, respectively.

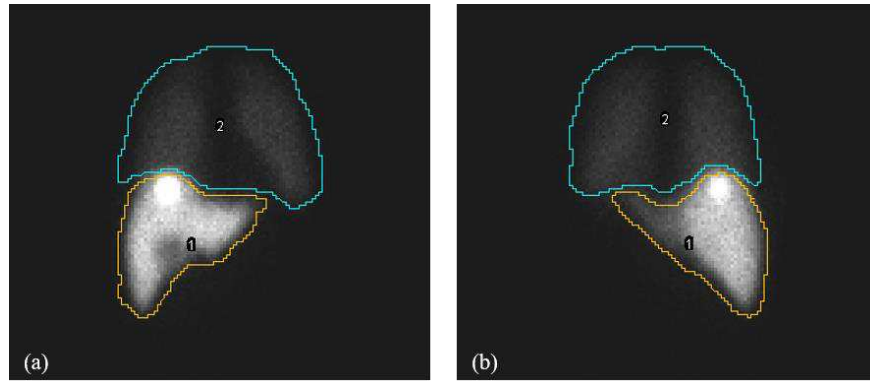
176

The LSF was then computed using Eq. 2.

177

$$LSF = \frac{GM_{lung}}{GM_{lung} + GM_{liver}} \quad (2)$$

178 where GM_{lung} and GM_{liver} are the geometric mean of the lungs and liver, respectively.



179

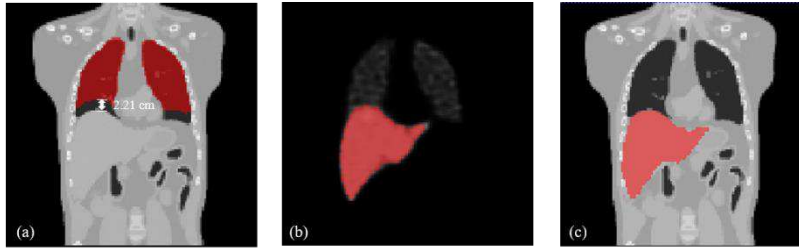
180 FIG. 4. Liver (orange ROI) and lung segmentation (blue ROI) of planar images on (a) anterior
181 and (b) posterior view.

182

183 For quantitative SPECT/CT images, an open-source semi-automatic software ITK-SNAP was
184 used for segmentation [25]. Lung volumes-of-interest (VOIs) were automatically segmented on
185 CT images by setting an upper threshold of -200 Hounsfield unit (HU), with manual removal of
186 the main trachea. To reduce the impact of respiratory motion spilling liver activity into the lungs,
187 an axial range of 2.21 cm of the basal lung VOI was excluded as shown in Fig. 5 (a) [6]. The
188 total lung counts can be estimated by the product of the lung mean count density (counts/voxel)
189 of the lung VOI after 2.21 cm exclusion and the original CT lung volume determined from each
190 CT protocol [7]. For liver segmentation, it can be done on the SPECT or CT images. Thus, liver
191 VOIs were segmented on SPECT images directly by setting a lower threshold of 2.5% of the
192 maximum count value (SPECT-based liver segmentation method) (Fig. 5b) [8] or contoured on
193 different CT images (Fig. 5c) and then mapped to the corresponding SPECT images (CT-based
194 liver segmentation method). The LSF on SPECT was calculated using Eq. 3.

195

$$LSF = \frac{lung\ counts}{liver\ counts + lung\ counts} \quad (3)$$



197

198 FIG. 5. (a) Lung segmentation with 2.21 cm axial exclusion on HCT-MID.(b) Liver
199 segmentation on SPECT image and on (c) HCT-MID for Phantom #1.

200

201 The SPECT-based or CT-based liver segmentation methods with lower mean absolute error
202 would then be applied to estimate LSF for different CT protocols.

203

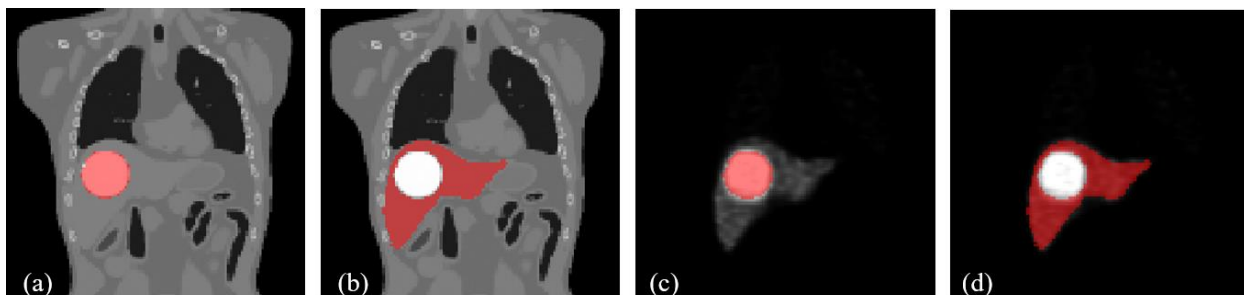
204 *TNR estimation*

205 Only ^{99m}Tc -MAA SPECT/CT images were used for TNR calculation. SPECT reconstructed
206 images using CACT for AC were first employed to investigate the best segmentation protocols
207 of the normal liver (NL) and tumor VOIs for TNR estimation. The tumor and NL VOIs were first
208 contoured on contrast HCT-IN, HCT-MID (Fig. 6a, b) and HCT-EX images respectively. The
209 tumor and NL VOIs would then be mapped to the SPECT images (Fig. 6c, d). The NL and tumor
210 VOIs can also be segmented from intensity thresholding on SPECT images. The whole liver was
211 segmented by setting a lower threshold of 2.5% of maximum intensity while the tumor was
212 segmented by setting a lower threshold of 40% (Fig. 7a) and 50% (Fig. 7c) of maximum
213 intensity on SPECT images, defined as SPECT(40%) and SPECT(50%), respectively. The NL
214 VOIs (Fig. 7b, d) were obtained by subtracting corresponding tumor VOIs from the whole liver
215 VOI. The third segmentation protocol was to delineate the NL and tumor VOIs by combining
216 information from SPECT and contrast HCT-EX images, i.e., SPECT+contrast HCT-EX protocol.

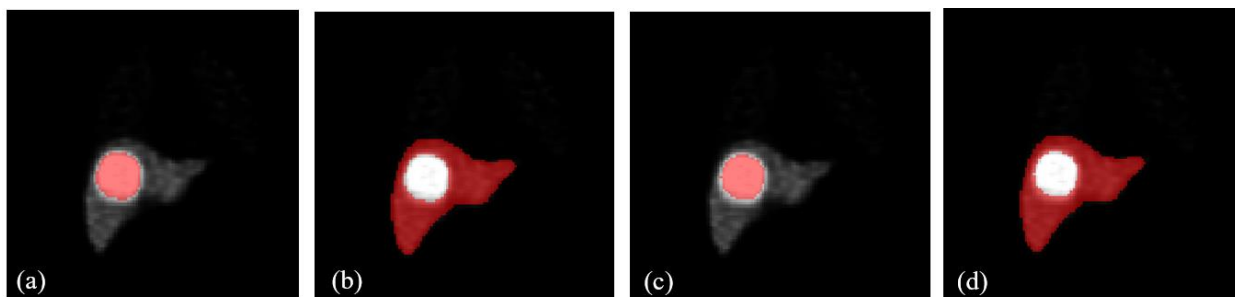
217 The NL (Fig. 8b) and tumor (Fig. 8a) VOIs were determined on SPECT images by setting a
218 threshold such that the volume of VOIs equaled to that of corresponding VOIs from the contrast
219 HCT-EX image [26]. The tumor and NL VOIs obtained from these methods can then be used to
220 calculate TNR using Eq. 4 [4, 27].

$$221 \quad \text{TNR} = \frac{\text{Activity_tumor}/\text{Mass_tumor}}{\text{Activity_NL}/\text{Mass_NL}} = \frac{\text{counts/voxel}_{\text{tumor}}}{\text{counts/voxel}_{\text{NL}}} \quad (4)$$

222 where counts/voxel is defined as mean count density.

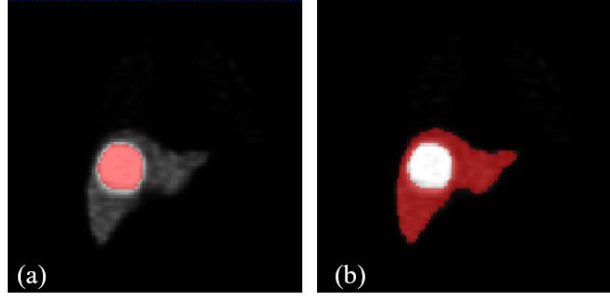


223
224 FIG. 6. (a) Tumor and (b) NL segmentation on contrast HCT-MID. Corresponding VOIs were
225 then mapped to segment the (c) tumor and (d) NL on SPECT images for Phantom #2.



226
227 FIG. 7. (a) Tumor segmented from 40% of maximum intensity and (b) corresponding NL VOI.
228 (c) Tumor segmented from 50% of maximum intensity and (d) corresponding NL VOI on
229 SPECT images for Phantom #2.

230



231
 232 FIG. 8. (a) Tumor and (b) NL VOIs on SPECT images such that their volumes equal to the
 233 volumes of corresponding VOIs from contrast HCT-EX for Phantom #2.

234
 235 The tumor and NL segmentation protocol with least mean absolute error of TNR estimation
 236 would then be applied to SPECT reconstructed images using different AC protocols for TNR
 237 calculation.

238
 239 ***Dosimetric evaluation***

240 According to the Medical Internal Radiation Dose committee, the radiation dose from ^{90}Y resin
 241 and glass microspheres to lungs, D_{lung} , can be computed by the following equation:

242
$$D_{lung} [\text{Gy}] = \frac{46.97 \times A_0 [\text{GBq}] \times LSF}{M [\text{kg}]} \quad (5)$$

243 where A_0 is the IA to the patient, i.e., assuming to be 3 GBq for dosimetric calculation in this
 244 study and M is the lung mass. For planar images, lung mass was assumed to be 1 kg as suggested
 245 [5] while for SPECT/CT images, it could be calculated by the product of the lung volume from
 246 corresponding CT images and lung density, i.e., 0.3 g/cm^3 [28].

247 The radiation dose to the NL (D_{NL}) and tumor (D_{tumor}) could be estimated by Eq. 6 and Eq. 7,
 248 respectively. The mass of NL and tumor could be calculated by the product of their volumes
 249 measured from the contrast HCT-EX image and soft tissue densities, i.e., 1.03 g/cm^3 ,

250 respectively [4, 29]. Only SPECT/CT data are used to calculate D_{NL} and D_{tumor} as TNR data are
251 not available for the planar protocol.

$$252 \quad D_{NL} \text{ [Gy]} = \frac{46.97 \times A_0 \text{ [GBq]} \times (1 - LSF)}{(M_{tumor} \text{ [kg]} \times TNR + M_{NL} \text{ [kg]})} \quad (6)$$

$$253 \quad D_{tumor} \text{ [Gy]} = \frac{46.97 \times A_0 \text{ [GBq]} \times (1 - LSF) \times TNR}{(M_{tumor} \text{ [kg]} \times TNR + M_{NL} \text{ [kg]})} \quad (7)$$

254 *Injected activity calculation*

255 The partition model with three compartments of lungs, NL and tumor was used to calculate IA in
256 this study [4]. To prevent the toxicity from lungs and NL, the maximum radiation dose to lungs
257 in this study was set to 25 Gy while the maximum NL absorbed dose was 80 Gy respectively.
258 After substituting the maximum lung absorbed dose into Eq. 5 to obtain the activity confined by
259 lungs and the limited NL absorbed dose into Eq. 6 for the activity confined by NL, the lower
260 activity value was selected as the IA.

261 The lung counts calculation in LSF, lung absorbed dose and IA calculations using Eq. 5
262 require the lung volume measurement which could be done using non-contrast CT of the
263 SPECT/CT scan. Notwithstanding, it is challenging to measure lung volume in CACT and IACT
264 due to their inherent motion blur (Fig. 3a, e). On the other hand, HCT-MID with clear organ
265 contour (Fig. 3c) could provide sharper boundaries for volume measurement with similar lung
266 size as compared to the corresponding SPECT. Therefore, in 4D CACT/IACT, one can extract
267 one HCT-MID/interpolated CT at mid-respiration (ICT-MID), for lung VOI segmentation
268 purpose. Such hybrid CT protocols were defined as CACT+HCT-MID and IACT+ICT-MID,
269 where CACT and IACT were used for AC while the extracted HCT-MID and IACT/ICT-MID
270 were used for lung VOI segmentation in LSF (and liver VOI segmentation if the estimation
271 results of CT-based could be better than SPECT-based liver segmentation), lung absorbed dose

272 and IA analysis to achieve better estimation. Additionally, as implied by Eqs. 6 and 7, the
273 absorbed dose calculation of NL and tumor is related to LSF and hence hybrid CT protocols are
274 applied.

275 The absolute errors of using planar and SPECT/CT protocols for LSF, TNR, lung, NL, tumor
276 absorbed dose and IA estimation for each phantom were calculated as compared to the ground
277 truth. A paired two-tailed t-test with Bonferroni correction was performed by SPSS Version 24
278 (IBM Corp., Armonk, NY, USA) between each protocol pair for different indices estimation
279 errors for 10 phantoms. A p value of <0.05 was regarded as statistically significant.

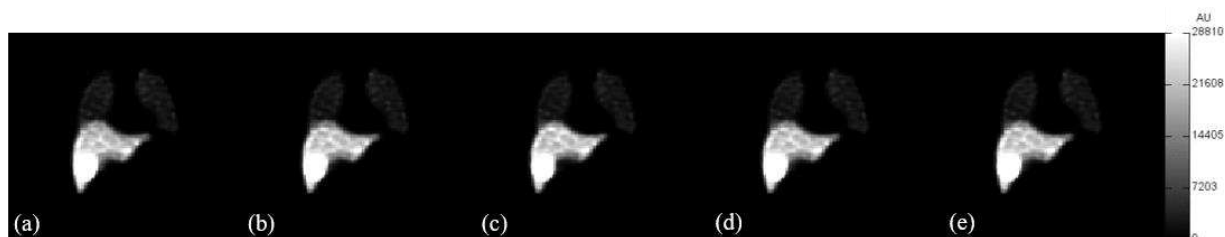
280

281 Results

282 SPECT reconstruction images using different CT protocols

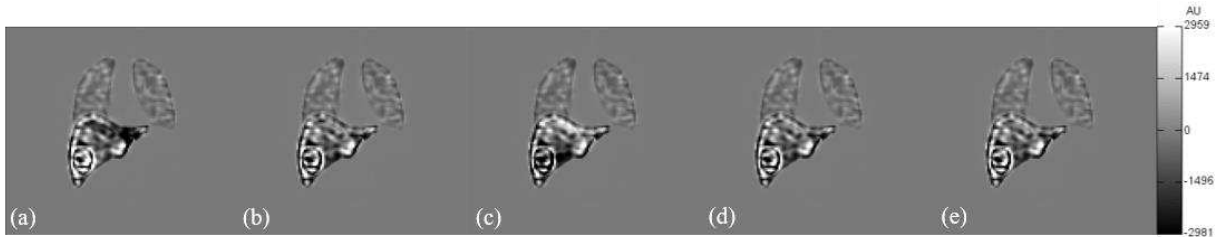
283 Figure 9 shows the reconstructed images of Phantom #9 with 20% LSF, using different
284 attenuation correction protocols. Figure 10 illustrates the difference images between these
285 reconstructed images and the true activity map. Therein, white and black regions represent the
286 overestimation and underestimation of counts, respectively.

287



288 FIG. 9. Reconstructed images of Phantom #9 with 20% LSF using (a) HCT-IN, (b) HCT-MID,
289 (c) HCT-EX, (d) CACT and (e) IACT for AC. AU: Arbitrary unit.

290



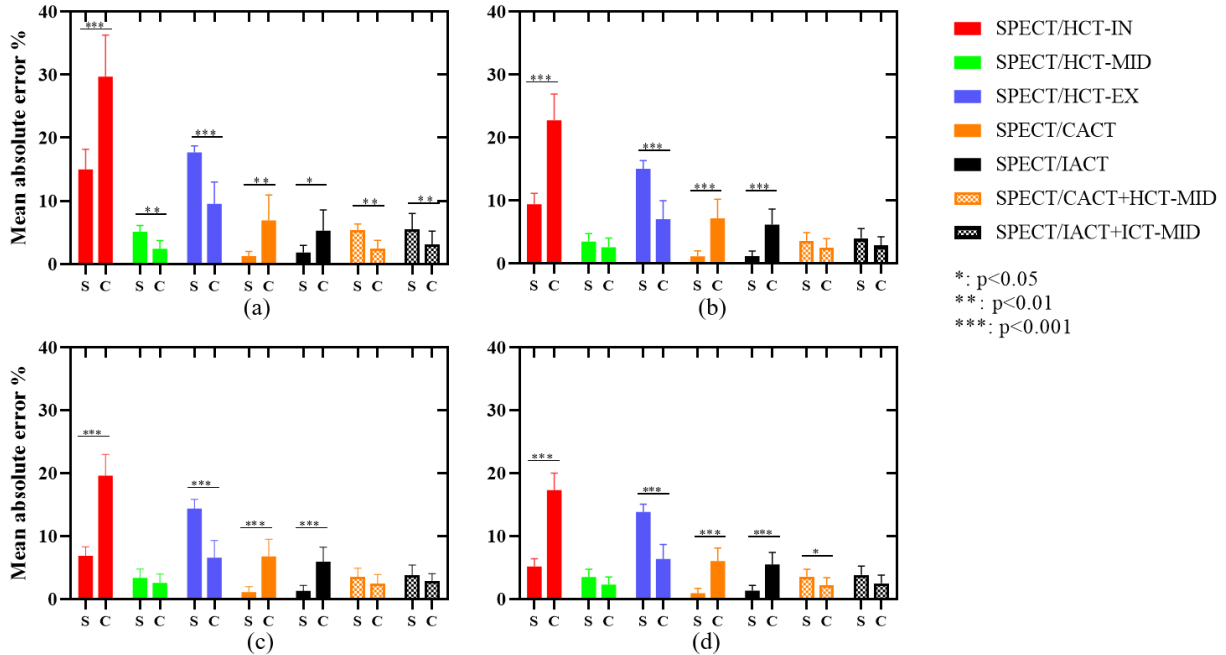
291
 292 FIG. 10. The difference images between reconstructed images of Phantom #9 with 20% LSF
 293 using (a) HCT-IN, (b) HCT-MID, (c) HCT-EX, (d) CACT and (e) IACT for AC and the true
 294 activity map. AU: Arbitrary unit.

295

296 **LSF estimation**

297 The absolute errors (mean \pm deviation) of SPECT- and CT-based liver segmentation on LSF
 298 estimation using different CT protocols for 10 phantoms are shown in Fig. 11. For SPECT/HCT-
 299 IN, SPECT/CACT and SPECT/IACT, SPECT-based liver segmentation has lower errors than
 300 CT-based liver segmentation. On contrary, CT-based liver segmentation has lower errors than
 301 SPECT-based liver segmentation for SPECT/HCT-MID, SPECT/HCT-EX and hybrid CT
 302 protocols, i.e., SPECT/CACT+HCT-MID and SPECT/IACT+ICT-MID where CACT/IACT is
 303 used for AC while HCT-MID/ICT-MID is used for segmentation. Generally, the mean absolute
 304 errors for all protocols decrease along with the increase of LSF. The superior segmentation
 305 method would be applied to the corresponding CT protocols to estimate LSF.

306



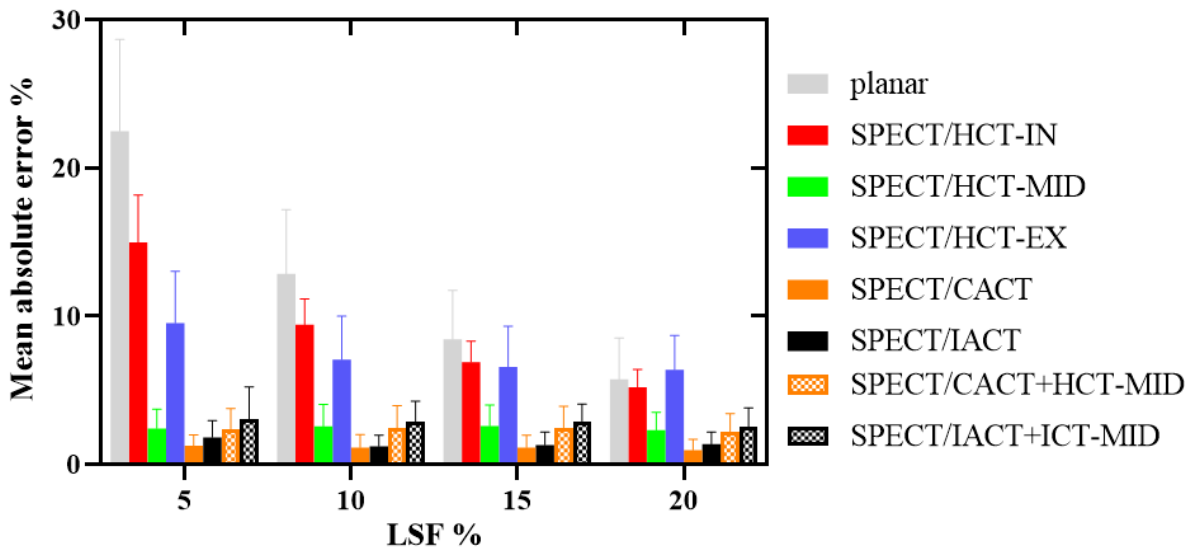
307

308 FIG. 11. The mean absolute errors of LSF estimation for different CT protocols using SPECT-
 309 and CT-based segmentation methods to segment liver for a LSF of (a) 5%, (b) 10%, (c) 15% and
 310 (d) 20%, respectively. S: SPECT-based segmentation, C: CT-based segmentation.

311

312 The mean absolute errors of LSF estimation from planar and SPECT images with different CT
 313 protocols for AC and VOI segmentation are shown in Fig. 12. Planar images considerably
 314 overestimate the LSF at lower LSF, with $21.85 \pm 6.81\%$, $12.84 \pm 4.33\%$, $8.43 \pm 3.30\%$, $5.73 \pm 2.78\%$
 315 mean absolute errors for LSF of 5%, 10%, 15% and 20%, respectively. SPECT/CACT has the
 316 best performance among all SPECT/CT protocols with the least mean absolute errors for LSF of
 317 5% ($1.25 \pm 0.74\%$), 10% ($1.13 \pm 0.88\%$), 15% ($1.12 \pm 0.85\%$) and 20% ($0.95 \pm 0.762\%$).
 318 SPECT/IACT is slightly inferior to SPECT/CACT with mean absolute errors of $1.82 \pm 1.13\%$,
 319 $1.20 \pm 0.77\%$, $1.30 \pm 0.87\%$ and $1.35 \pm 0.83\%$ for LSF of 5%, 10%, 15% and 20%, respectively.
 320 SPECT/HCT-MID has the best performance out of SPECT/HCTs in LSF estimation. The errors
 321 from hybrid CT protocols, i.e., SPECT/CACT+HCT-MID and SPECT/IACT+HCT-MID, are

322 about 1% higher than SPECT/CACT and SPECT/IACT respectively, and are similar to
 323 SPECT/HCT-MID. Generally, the mean absolute errors for all protocols decrease along with the
 324 increase of LSF. Except SPECT/HCT-EX, other SPECT/CTs and planar imaging overestimate
 325 the LSFs. The errors of planar and SPECT/HCT-IN protocols are statistically significantly higher
 326 than SPECT/CACT, SPECT/IACT, SPECT/HCT-MID and hybrid CT protocols for all LSFs.

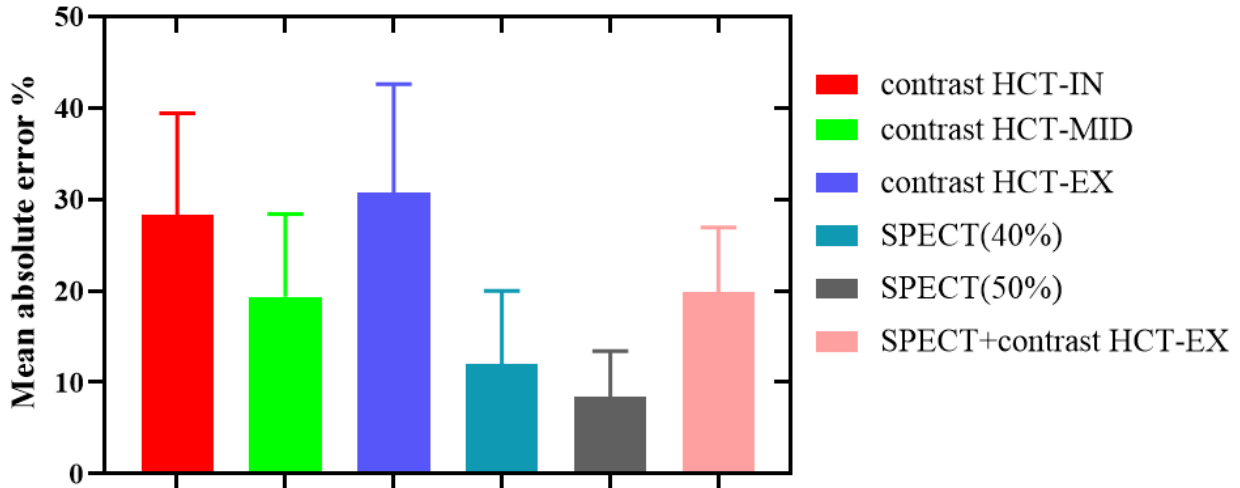


327
 328 FIG. 12. The mean absolute errors of LSF estimation from SPECT images with different CT
 329 protocols for AC and VOI segmentation.

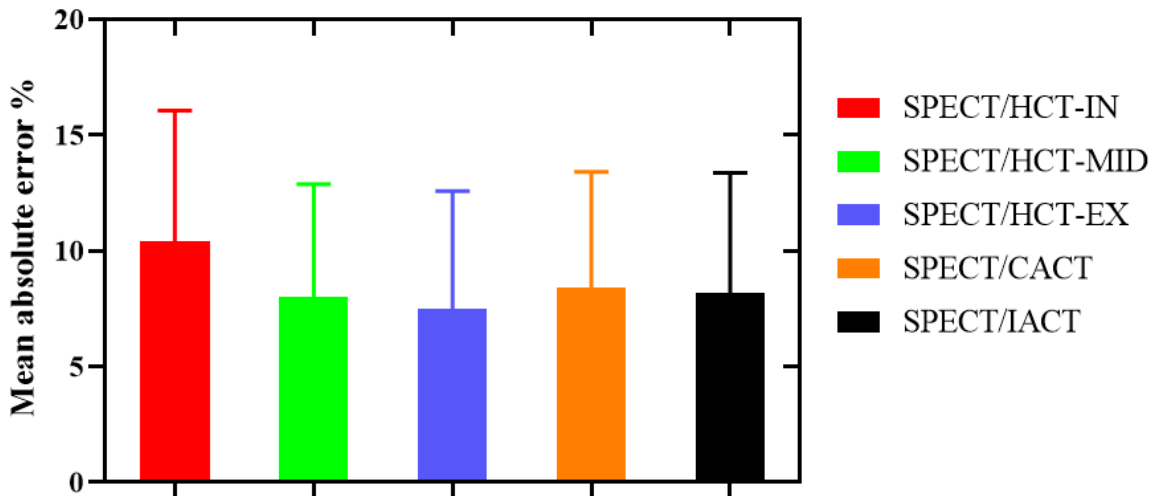
330
 331 **TNR estimation**

332 For different tumor and NL segmentation protocols performed on SPECT/CACT images, their
 333 mean absolute errors are shown in Fig. 13. SPECT(50%) segmentation protocol has the
 334 significantly lower mean absolute error of $8.43 \pm 5.00\%$, which was later applied to SPECT
 335 reconstructed images using different CT protocols for AC to estimate the TNR in this study (Fig.
 336 14). Results are similar for different LSFs thus only results for LSF of 5% are shown.
 337 SPECT/HCT-IN has the highest TNR errors of $10.42 \pm 5.65\%$ while for other SPECT/CT images,

338 their mean absolute errors of TNR estimation are similar, about $8.00 \pm 5.00\%$. There is no
339 statistically significant difference between each AC protocol pair.



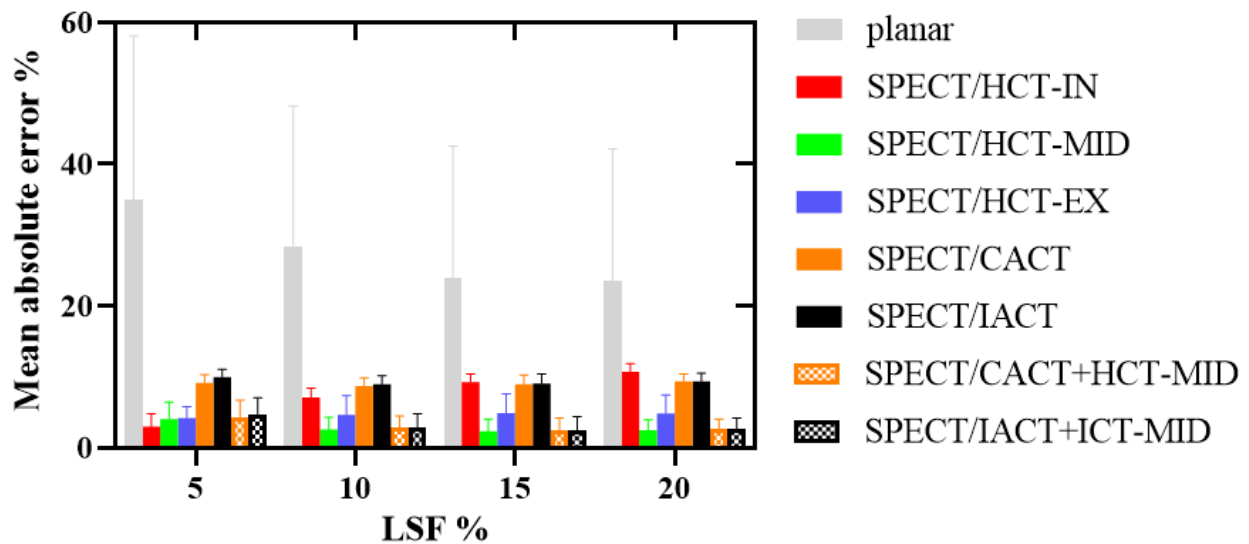
340
341 FIG. 13. The mean absolute errors of TNR estimation for different tumor and NL segmentation
342 methods for a LSF of 5%.



343
344 FIG. 14. The mean absolute errors of TNR estimation from SPECT images with different AC
345 protocols using SPECT(50%) segmentation method for a LSF of 5%.

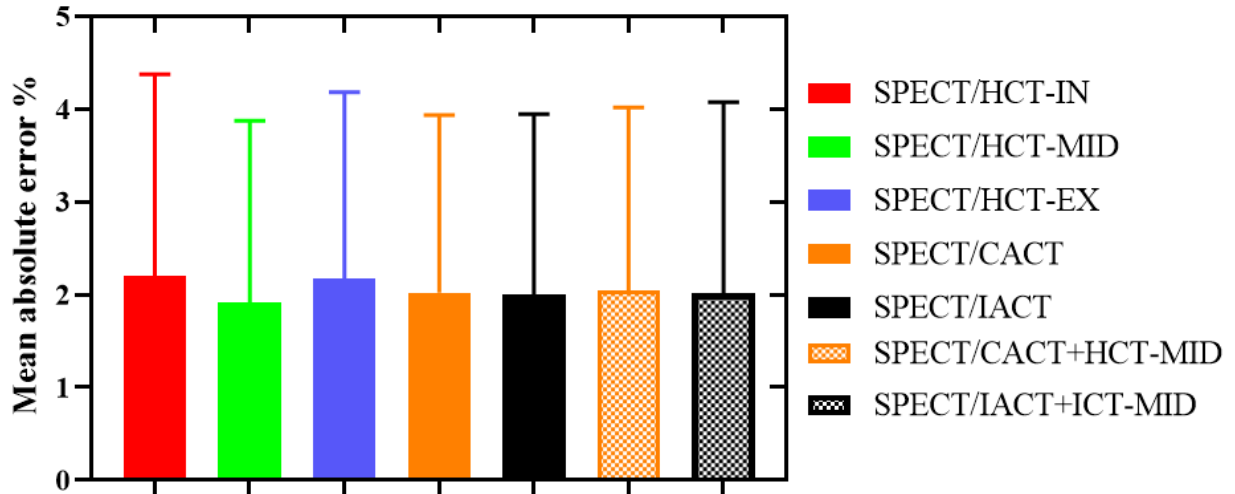
346
347 **Dosimetric evaluation**

348 The mean absolute errors for the lung absorbed dose are presented in Fig. 15. Compared to
 349 SPECT/CT protocols, planar images highly overestimate the lung absorbed dose, with mean
 350 absolute errors of up to $34.42 \pm 23.84\%$ for LSF of 5%, and their errors are statistically
 351 significantly higher than those of SPECT/HCT-MID and hybrid CT protocols for all LSFs. On
 352 the other hand, all SPECT/CT protocols underestimate lung absorbed dose except SPECT/HCT-
 353 EX. SPECT/HCT-IN shows least mean absolute errors of lung absorbed dose for LSF of 5%
 354 ($2.97 \pm 1.80\%$) but its errors increase as the LSF increase. SPECT/HCT-MID and hybrid CT
 355 protocols have significantly lower errors for LSF of 10% ($\sim 2.60 \pm 1.80\%$), 15% ($\sim 2.50 \pm 1.80\%$),
 356 and 20% ($\sim 2.50 \pm 1.50\%$) as compared to SPECT/HCT-IN, SPECT/CACT and SPECT/IACT.



357
 358 FIG. 15. The mean absolute errors of lung absorbed dose estimation for 10 phantoms.

359
 360 For NL absorbed dose estimation, the mean and standard deviation of absolute errors from
 361 different CT protocols over all LSFs are similar ($\sim 2.00 \pm 2.00\%$) without significant difference
 362 and results of LSF=5% is shown in Fig. 16. It tends to be overestimated (~ 8 out of 10 phantoms)
 363 for all LSFs and protocols.

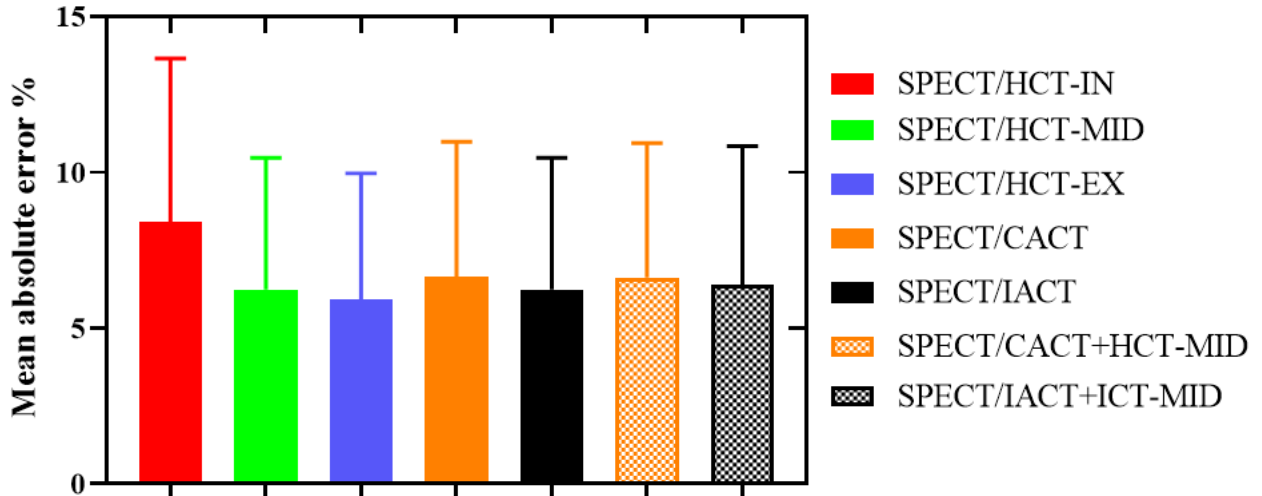


364

365 FIG. 16. The mean absolute errors of NL absorbed dose estimation for 10 phantoms with LSF of
 366 5%.

367

368 For tumor absorbed dose estimation, the mean and standard deviation of absolute errors from
 369 10 phantoms with LSF of 5% is shown in Fig. 17. Results are also similar for different LSFs.
 370 SPECT/HCT-IN has a slightly higher error with $8.41 \pm 5.24\%$ than others ($\sim 6.00 \pm 4.00\%$). There
 371 is no significant difference between each CT protocol pair. In contrast to NL absorbed dose,
 372 tumor absorbed dose tends to be underestimated (~ 8 out of 10 phantoms) for all LSFs and
 373 protocols.



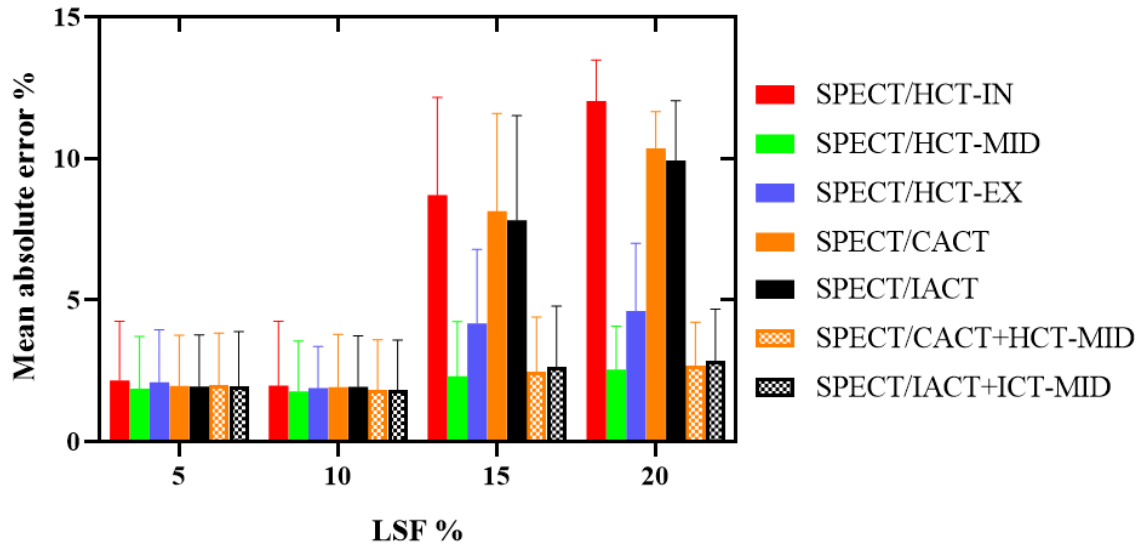
374

375 FIG. 17. The mean absolute errors of tumor absorbed dose estimation for 10 phantoms with LSF
 376 of 5%.

377

378 **Injected activity estimation**

379 Fig. 18 shows the mean and standard deviation of absolute errors of IA of 10 phantoms. The
 380 errors of all SPECT/CT images with LSFs of 5% and 10% are generally lower than those with
 381 LSFs of 15% and 20%. For lower LSFs ($LSF \leq 10\%$), IA tends to be underestimated (~8 out of
 382 10 phantoms), and all protocols have similar performance without statistically significant
 383 difference. For LSF of 15% and 20%, SPECT/HCT-IN results in highest IA estimation errors,
 384 reaching $8.70 \pm 3.45\%$ and $12.03 \pm 1.44\%$ correspondingly while SPECT/HCT-MID and hybrid
 385 CT protocols show statistically better results compared to other protocols.



386

387 FIG. 18. The mean absolute errors of IA estimation from 10 phantoms.

388

389 Discussion

390 Although Yu et al. [6] and Allred et al. [22] had already related AC to the accuracy of lung
 391 absorbed dose and LSF, they did not compare the effect of different AC maps in details.
 392 Dittmann et al. [8] proposed using breath hold during CT and shallow breathing during SPECT
 393 to reduce the respiratory artifact in ^{99m}Tc -MAA SPECT, but there is a lack of clear criterion for
 394 shallow breathing. Our study systemically evaluated various CT protocols for clinical ^{99m}Tc -
 395 MAA SPECT AC and segmentation reference. For HCT-IN, liver moves down due to lung
 396 expansion resulting in underestimation of the top part of the liver activity (Fig. 10a) by
 397 incorrectly using the attenuation coefficient of lungs for AC. For HCT-EX, the liver goes up
 398 because of lung compression, leading to overestimation of the basal part of lungs activity (Fig.
 399 10c) by incorrectly using the attenuation coefficient of the liver for AC. This problem can be
 400 alleviated using HCT-MID as the AC map. Indeed, in the lung-liver interface on static SPECT,

401 AC would require a mixture of lungs and liver attenuation coefficients in the lungs-liver border
402 due to the motion blur. The average CTs, i.e., CACT and IACT, which average different states of
403 respiration, can meet this requirement. Comparing with CACT, IACT is slightly inferior in
404 image quality but can be generated with lower radiation exposure, with only two HCTs acquired
405 in end-inspiration and end-expiration phases aided by an active breathing controller [14]. Our
406 results, as expected, showed that compared to SPECT/CT images, ^{99m}Tc -MAA planar images
407 overestimate the LSF even with 1 cm exclusion of ROIs in the lung-liver interface, probably
408 attributed to the lack of AC, SC, CDR compensation and 3D information. The LSF errors from
409 planar images without 1 cm exclusion of ROIs are about 10% higher than those with exclusion
410 for each LSF setting (data not shown). The results are consistent with previous studies [6-8, 22].

411 Segmentation of lungs, liver and tumor is essential for both LSF, TNR and dosimetric analyses
412 while breathing motion has significant impact on segmentation. For LSF estimation, the 2.21 cm
413 exclusion segmentation method is suitable for HCT-MID, CACT and IACT to exclude the
414 motion artifact. However, even with exclusion, HCT-IN tends to overestimate the lung volume
415 while HCT-EX tends to underestimate it, which could be implied in Fig. 3(b) and (d). As a result,
416 SPECT/HCT-IN overestimates the LSF while SPECT/HCT-EX underestimates it even with their
417 own best liver segmentation method. Due to the motion blur, CACT and IACT also slightly
418 overestimate the lung volume but they preserve the lung counts better than other methods.
419 Meanwhile, the SPECT-based liver segmentation by setting lower threshold of 2.5% of
420 maximum also preserves liver counts, resulting in good performance of CACT and IACT for
421 LSF estimation. Thresholds of 2%, 2.5%, 3%, 3.5% and 4% of maximum intensity have been
422 investigated and while threshold of 2.5% showed the best result thus is used in this study (data
423 not shown).

424 The use of SPECT with a good AC and segmentation protocol, i.e., CACT, IACT, HCT-MID
425 or hybrid CT protocols, could possibly change the patient management as planar and
426 SPECT/HCT-IN overestimates the LSFs, which may lead to prohibiting certain patients for the
427 subsequent ⁹⁰Y radioembolization while SPECT/HCT-EX underestimates the LSFs, resulting in
428 putting some patients at risk based on the 20% LSF cutoff criteria [5]. Using mismatched AC
429 maps and segmentation protocols can even lead to similar LSF errors as compared to planar for
430 higher LSF, i.e., HCT-EX and HCT-IN for $LSF \geq 15\%$.

431 For NL and tumor VOIs segmentation in TNR estimation, using SPECT images has proven to
432 be more accurate than using contrast CT images in this study. However, the volume of NL and
433 tumor VOIs segmented from SPECT images are inaccurate due to the inferior image quality.
434 Thus, contrast CT images are utilized to perform the NL and tumor volume measurement in IA,
435 NL and tumor absorbed dose calculation while the non-contrast CT for AC does not provide
436 sufficient soft tissue contrast for these tasks. Contrast HCT-IN and HCT-EX are misaligned with
437 SPECT images resulting in highest TNR estimation errors compared to other segmentation
438 protocols. Meanwhile, contrast HCT-MID and SPECT+contrast HCT-EX segmentation
439 protocols register better with SPECT images but the blurred boundary of the tumor on SPECT
440 images due to respiration is included, leading to inaccurate tumor mean count density while
441 SPECT image segmentation protocols with an appropriate threshold setting can alleviate this
442 problem. In Fig. 14, different AC protocols for TNR estimation have similar performance given
443 the best segmentation method, since the lung-liver interface accounting for a relatively small
444 portion of the whole NL. Additionally, the SPECT-based segmentation method also reduces the
445 impact of AC protocols for tumor mean count density estimation. The same trend was found for
446 specific phantoms with tumor close to the lung-liver interface (data not shown).

447 Dosimetric and IA estimation are affected by multiple factors, including LSF, compartment
448 mass measurements and TNR according to the partition model, which make the results rather
449 complex. For lung absorbed dose estimation, planar protocols are the worst compared to other
450 SPECT/CT protocols due to inaccurate LSF estimation and standard lung mass assumption of 1
451 kg. The error of average CTs is mainly due to incorrect lung mass measurement. Unexpectedly,
452 SPECT/HCT-IN shows good results in low LSF while SPECT/HCT-EX shows good results
453 generally, although they are both inaccurate in LSF and lung mass measurement. The concurrent
454 overestimation of LSF and lung mass measurement from SPECT/HCT-IN and the
455 underestimation of those from SPECT/HCT-EX result in lower lung absorbed dose error
456 according to Eq. 5. As a result, the performance of SPECT/HCT-IN is not stable along with the
457 changing of LSF. On the contrary, hybrid CT protocols and SPECT/HCT-MID are generally
458 stable as a result of more accurate LSF and lung mass measurement. On the other hand, lung
459 mass measurement may be further improved using lung CT densitovolumetry method proposed
460 by Kao et al. [7].

461 For absorbed dose of NL and tumor, they are generally good due to low errors of TNR
462 estimation as well as low errors of NL and tumor mass measurement from the contrast CT
463 according to Eqs. 6 and 7. Moreover, the errors of NL absorbed dose are generally lower than
464 those of tumor absorbed dose, attributed to a larger volume of NL that is less sensitive to volume
465 measurement errors as compared to the tumor.

466 For IA estimation in Fig. 18, since the NL absorbed dose limitation is the dominant factor for
467 low LSF (<10%), the IA estimation error is generally low as a result of low errors of NL
468 absorbed dose (Fig. 16). Along with the increase of LSF, the influence of LSF increases, leading
469 to the similar order of IA errors for different CT protocols to that of lung absorbed dose errors,

470 where the hybrid CT protocols and SPECT/HCT-MID provide the best results. Besides, lower
471 LSF ($\leq 10\%$) is more common in the clinic [8, 22]. Thus, different AC protocols are comparable
472 for estimating IA.

473 The treatment planning results from HCT-MID and hybrid CT protocols are generally good
474 and more stable compared to other protocols. However, similar to IACT, the HCT-MID
475 acquisition would require the aid of an active breathing controller as it is difficult to have
476 patients suspended their breath during mid-respiratory phase. In an ideal situation, shallow free
477 breathing CT may have similar performance as compared to HCT-MID but that would highly
478 depend on patients' compliance. Meanwhile, 4D CT protocols may be more feasible in clinic,
479 where CACT could be used to perform AC in SPECT reconstruction while an HCT in middle-
480 respiration phase could be extracted from CACT for VOI segmentation propose. However,
481 higher radiation dose would be expected. If 4D CT or HCT-MID could not be realized,
482 SPECT/HCT-EX is also a reasonable choice as compared to SPECT/HCT-IN and planar imaging.

483 Respiratory motion affects the quantitative measurement in static ^{99m}Tc -MAA SPECT and
484 could be potentially improved by respiratory gating method, which is currently under
485 investigation in our laboratory. Moreover, recent studies pointed out that ^{99m}Tc -MAA was not
486 perfectly reliable in modelling ^{90}Y microsphere distribution as the size and injected activity for
487 ^{99m}Tc -MAA microspheres could be not exactly the same from ^{90}Y microspheres (^{99m}Tc -MAA:
488 mean diameter of 10-40 μm , SIR-Sphere: mean diameter of 20-60 μm , TheraSphere: mean
489 diameter of 20-30 μm) [30, 31]. Therefore, ^{90}Y post-treatment imaging-based dosimetry should
490 be conducted to confirm the parameters estimated by ^{99m}Tc -MAA. The effect of breathing
491 motion, mismatch artifacts and segmentation accuracy may not have the same magnitude on ^{90}Y
492 bremsstrahlung imaging/CT, as the image quality and quantitative accuracy are generally poor

493 for bremsstrahlung imaging. However, ^{90}Y PET/CT provides higher image resolution [32, 33]
494 where respiratory motion, AC mismatch and segmentation could be more of a problem. Further
495 evaluation of our results using clinical $^{99\text{m}}\text{Tc}$ -MAA SPECT/CT, ^{90}Y bremsstrahlung imaging/CT
496 and ^{90}Y PET/CT patient data are beyond the scope of this study and need other independent
497 investigations.

498

499 **Conclusions**

500 The choice of CT in $^{99\text{m}}\text{Tc}$ -MAA SPECT/CT affects both AC and segmentation accuracy. Our
501 results showed that the LSF derived from $^{99\text{m}}\text{Tc}$ -MAA planar images is inferior to those obtained
502 from SPECT/CT images with good AC and segmentation methods. The LSF, TNR, absorbed
503 dose and IA estimation of $^{99\text{m}}\text{Tc}$ -MAA SPECT/CT could be further improved by the use of 4D
504 CT protocols in terms of AC and segmentation for personalized ^{90}Y microsphere treatment
505 planning. Helical CT acquired at end-expiration would also be a recommended choice if 4D CT
506 option is not available.

507

508 **Abbreviations**

509 AC: Attenuation correction; CACT: Cine average computed tomography; CDR: Collimator-
510 detector response; GM: Geometric mean; HCC: Hepatocellular carcinoma; HCT: Helical CT;
511 HCT-EX: Helical computed tomography acquired at end-expiration; HCT-IN: Helical computed
512 tomography acquired at end-inspiration; HCT-MID: Helical computed tomography acquired at
513 mid-respiration; HU: Hounsfield unit; IA: Injected activity; IACT: Interpolated average
514 computed tomography; ICT-MID: Interpolated computed tomography at mid-respiration; LEHR:

515 Low energy high resolution; LSF: Lung shunting fraction; NL: Normal liver; NSD: Normalized
516 standard deviation; OS-EM: Ordered subset expectation maximization; PET/CT: Positron
517 emission tomography/computed tomography; ROI: Region-of-interest; SC: Scatter correction;
518 SIRT: Selective internal radiation therapy; SPECT/CT: Single-photon emission computed
519 tomography/computed tomography; TNR: Tumor-to-normal liver ratio; ^{99m}Tc-MAA: ^{99m}Tc-
520 macroaggregated albumin; VOI: Volume-of-interest; XCAT: 4D digital extended cardiac torso

521

522 **Acknowledgements**

523 We thank former lab members, Drs. Duo Zhang and Ilker Ozsahin for proofreading the
524 manuscript, and Mr. Jianying Lee from Taipei Veterans General Hospital for providing clinical
525 information.

526

527 **Authors' contributions**

528 ZL LU and Greta Mok were both the primary writers of the manuscript. ZL LU was mainly
529 responsible for phantom generation, data collection and analysis while Greta Mok was
530 responsible for the simulation design, data interpretation and study integration.

531

532 **Funding**

533 This work was supported by the research grant from University of Macau (MYRG2017-00060-
534 FST).

535

536 **Availability of data and materials**

537 The datasets used and analyzed during the current study are available from the corresponding

538 author on reasonable request.

539

540 **Ethics approval and consent to participate**

541 Not applicable.

542

543 **Consent for publication**

544 Not applicable.

545

546 **Competing interests**

547 The authors declare that they have no competing interests.

548

549 **Reference**

550 1. Salem R, Lewandowski RJ, Kulik L, Wang E, Riaz A, Ryu RK, et al. Radioembolization results in longer
551 time-to-progression and reduced toxicity compared with chemoembolization in patients with hepatocellular
552 carcinoma. *Gastroenterology*. 2011;140:497-507 e2.

553 2. Sarfaraz M, Kennedy AS, Cao ZJ, Sackett GD, Yu CX, Lodge MA, et al. Physical aspects of yttrium-90
554 microsphere therapy for nonresectable hepatic tumors. *Med Phys*. 2003;30:199-203.

555 3. Riaz A, Awais R, Salem R. Side effects of yttrium-90 radioembolization. *Front Oncol*. 2014;4:198.
556 <https://doi.org/10.3389/fonc.2014.00198>.

557 4. Ho S, Lau WY, Leung TW, Chan M, Ngar YK, Johnson PJ, et al. Partition model for estimating radiation
558 doses from yttrium-90 microspheres in treating hepatic tumours. *Eur J Nucl Med*. 1996;23:947-52.

559 5. Garin E, Rolland Y, Laffont S, Edeline J. Clinical impact of (99m)Tc-MAA SPECT/CT-based dosimetry in
560 the radioembolization of liver malignancies with (90)Y-loaded microspheres. *Eur J Nucl Med Mol Imaging*.
561 2016;43:559-75. <https://doi.org/10.1007/s00259-015-3157-8>.

562 6. Yu N, Srinivas SM, Difilippo FP, Shrikanthan S, Levitin A, McLennan G, et al. Lung dose calculation with
563 SPECT/CT for (90)Yttrium radioembolization of liver cancer. *Int J Radiat Oncol Biol Phys.* 2013;85:834-9.

564 7. Kao YH, Magsombol BM, Toh Y, Tay KH, Chow P, Goh AS, et al. Personalized predictive lung dosimetry
565 by technetium-99m macroaggregated albumin SPECT/CT for yttrium-90 radioembolization. *EJNMMI Res.*
566 2014;4:33. <https://doi.org/10.1186/s13550-014-0033-7>.

567 8. Dittmann H, Kopp D, Kupferschlaeger J, Feil D, Groezinger G, Syha R, et al. A Prospective Study of
568 Quantitative SPECT/CT for Evaluation of Lung Shunt Fraction Before SIRT of Liver Tumors. *J Nucl Med.*
569 2018;59:1366-72.

570 9. Segars WP, Tsui BM, editors. Effect of respiratory motion in CT-based attenuation correction in SPECT
571 using different CT scanners and protocols. *IEEE Nuclear Science Symposium Conference Record.* 2005;doi:
572 10.1109/NSSMIC.2005.1596819.

573 10. McQuaid SJ, Hutton BF. Sources of attenuation-correction artefacts in cardiac PET/CT and SPECT/CT.
574 *Eur J Nucl Med Mol Imaging.* 2008;35:1117-23.

575 11. Zhang D, Yang BH, Wu NY, Mok GS. Respiratory average CT for attenuation correction in myocardial
576 perfusion SPECT/CT. *Ann Nucl Med.* 2017;31:172-80.

577 12. Zhang D, Ghaly M, Mok GSP. Interpolated CT for attenuation correction on respiratory gating cardiac
578 SPECT/CT - A simulation study. *Med Phys.* 2019;46:2621-8.

579 13. Mok GS, Ho CY, Yang B-H, Wu T-H. Interpolated average CT for cardiac PET/CT attenuation correction.
580 *J Nucl Cardiol.* 2016;23:1072-9.

581 14. Sun T, Wu TH, Wang SJ, Yang BH, Wu NY, Mok GS. Low dose interpolated average CT for thoracic
582 PET/CT attenuation correction using an active breathing controller. *Med Phys.* 2013;40:102507.

583 15. Ho CY, Wu T-H, Mok GS. Interpolated average CT for PET attenuation correction in different lesion
584 characteristics. *Nucl Med Commun.* 2016;37:297-306.

585 16. Bastiaannet R, Kappadath SC, Kunnen B, Braat AJAT, Lam MGEH, de Jong HWAM. The physics of
586 radioembolization. *EJNMMI Physics.* 2018;5:22. <https://doi.org/10.1186/s40658-018-0221-z>.

587 17. Segars WP, Sturgeon G, Mendonca S, Grimes J, Tsui BM. 4D XCAT phantom for multimodality imaging
588 research. *Med Phys.* 2010;37:4902-15.

- 589 18. Ghaly M, Du Y, Fung GS, Tsui BM, Links JM, Frey E. Design of a digital phantom population for
590 myocardial perfusion SPECT imaging research. *Phys Med Biol.* 2014;59:2935.
- 591 19. Ho CL, Chen S, Cheung SK, Leung YL, Cheng KC, Wong KN, et al. Radioembolization with (90)Y glass
592 microspheres for hepatocellular carcinoma: significance of pretreatment (11)C-acetate and (18)F-FDG PET/CT and
593 posttreatment (90)Y PET/CT in individualized dose prescription. *Eur J Nucl Med Mol Imaging.* 2018;45:2110-21.
- 594 20. Frey E, Tsui B. A practical method for incorporating scatter in a projector-backprojector for accurate
595 scatter compensation in SPECT. *IEEE Transactions on Nuclear Science.* 1993;40:1107-16.
- 596 21. Frey EC, Tsui B, editors. A new method for modeling the spatially-variant, object-dependent scatter
597 response function in SPECT. 1996 IEEE Nuclear Science Symposium Conference Record. 1996;doi:
598 10.1109/NSSMIC.1996.591559.
- 599 22. Allred JD, Niedbala J, Mikell JK, Owen D, Frey KA, Dewaraja YK. The value of (99m)Tc-MAA
600 SPECT/CT for lung shunt estimation in (90)Y radioembolization: a phantom and patient study. *EJNMMI Res.*
601 2018;8:50. <https://doi.org/10.1186/s13550-018-0402-8>.
- 602 23. Mok GS, Sun T, Huang TC, Vai MI. Interpolated average CT for attenuation correction in PET--a
603 simulation study. *IEEE Trans Biomed Eng.* 2013;60:1927-34.
- 604 24. Huang TC, Mok GS, Wang SJ, Wu TH, Zhang G. Attenuation correction of PET images with interpolated
605 average CT for thoracic tumors. *Phys Med Biol.* 2011;56:2559-67.
- 606 25. Yushkevich PA, Piven J, Hazlett HC, Smith RG, Ho S, Gee JC, et al. User-guided 3D active contour
607 segmentation of anatomical structures: significantly improved efficiency and reliability. *Neuroimage.* 2006;31:1116-
608 28.
- 609 26. Bastiaannet R, Viergever MA, de Jong HW. Impact of respiratory motion and acquisition settings on
610 SPECT liver dosimetry for radioembolization. *Med Phys.* 2017;44:5270-9.
- 611 27. Chansanti O, Jahangiri Y, Matsui Y, Adachi A, Geeratikun Y, Kaufman JA, et al. Tumor Dose Response in
612 Yttrium-90 Resin Microsphere Embolization for Neuroendocrine Liver Metastases: A Tumor-Specific Analysis with
613 Dose Estimation Using SPECT-CT. *J Vasc Interv Radiol.* 2017;28:1528-35.
- 614 28. Van Dyk J, Keane TJ, Rider WD. Lung density as measured by computerized tomography: implications for
615 radiotherapy. *Int J Radiat Oncol Biol Phys.* 1982;8:1363-72.

- 616 29. Gulec SA, Mesoloras G, Stabin M. Dosimetric techniques in ⁹⁰Y-microsphere therapy of liver cancer: The
617 MIRD equations for dose calculations. *J Nucl Med.* 2006;47:1209-11.
- 618 30. Elschot M, Nijssen JF, Lam MG, Smits ML, Prince JF, Viergever MA, et al. (^{99m}Tc)-MAA overestimates
619 the absorbed dose to the lungs in radioembolization: a quantitative evaluation in patients treated with (¹⁶⁶Ho)-
620 microspheres. *Eur J Nucl Med Mol Imaging.* 2014;41:1965-75.
- 621 31. Wondergem M, Smits ML, Elschot M, de Jong HW, Verkooijen HM, van den Bosch MA, et al. ^{99m}Tc-
622 macroaggregated albumin poorly predicts the intrahepatic distribution of ⁹⁰Y resin microspheres in hepatic
623 radioembolization. *J Nucl Med.* 2013;54:1294-301. <https://doi.org/10.2967/jnumed.112.117614>.
- 624 32. Yue J, Mauxion T, Reyes DK, Lodge MA, Hobbs RF, Rong X, et al. Comparison of quantitative Y-90
625 SPECT and non-time-of-flight PET imaging in post-therapy radioembolization of liver cancer. *Med Phys.*
626 2016;43:5779.
- 627 33. Elschot M, Vermolen BJ, Lam MG, de Keizer B, van den Bosch MA, de Jong HW. Quantitative
628 comparison of PET and Bremsstrahlung SPECT for imaging the in vivo yttrium-90 microsphere distribution after
629 liver radioembolization. *PLoS One.* 2013;8:e55742. <https://doi.org/10.1371/journal.pone.0055742>.
- 630

Figures

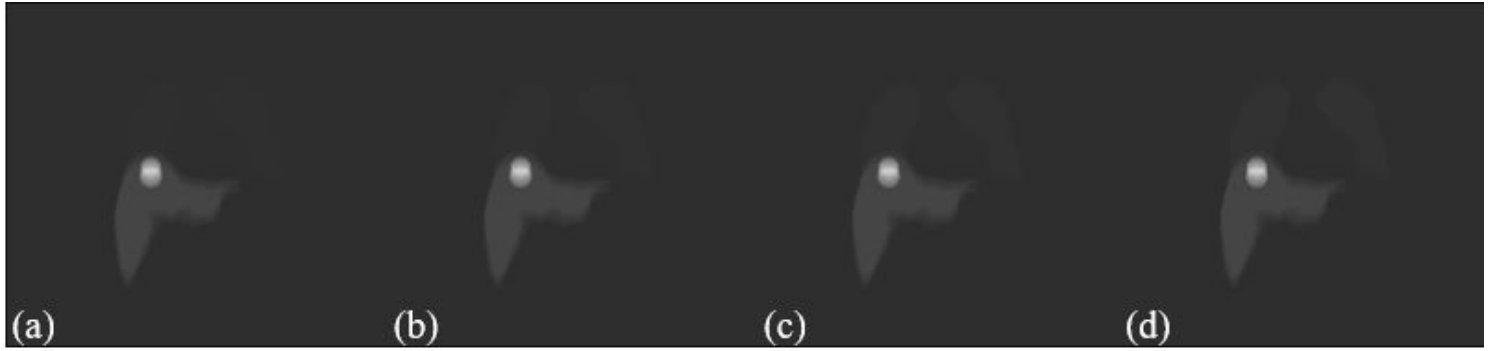


Figure 1

Phantom #6 with LSF of (a) 5%, (b) 10%, (c) 15% and (d) 20%.

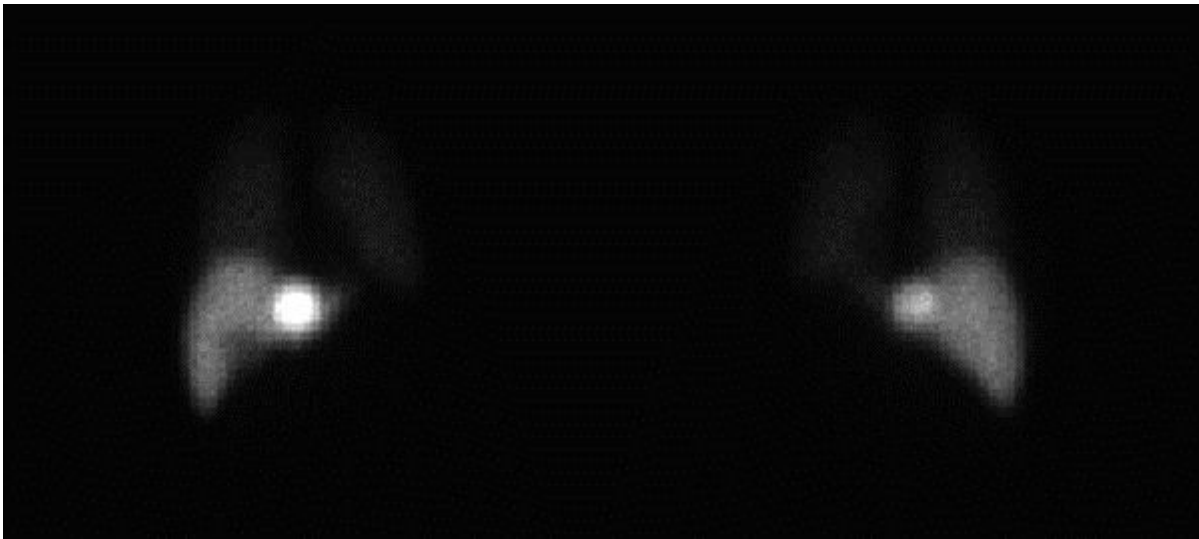


Figure 2

Noisy anterior (left) and posterior (right) planar images of Phantom #3.

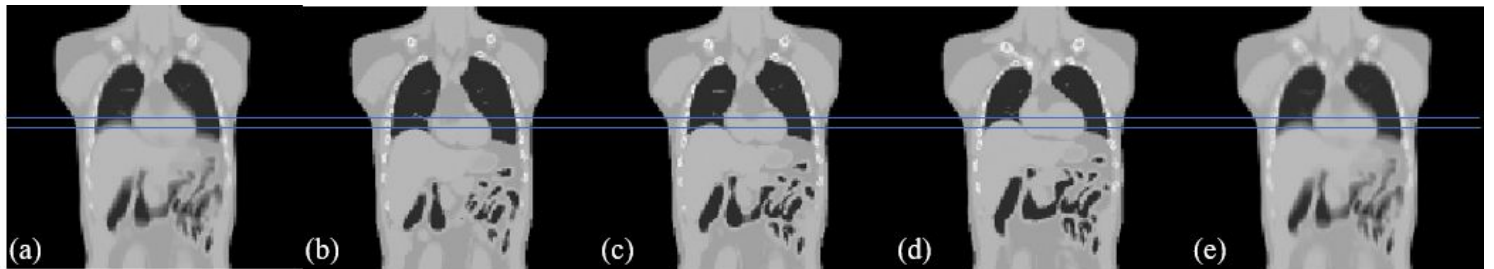


Figure 3

(a) CACT, (b) HCT-IN, (c) HCT-MID, (d) HCT-EX and (e) IACT of Phantom #1. Blue lines represent motion range of 2 cm.

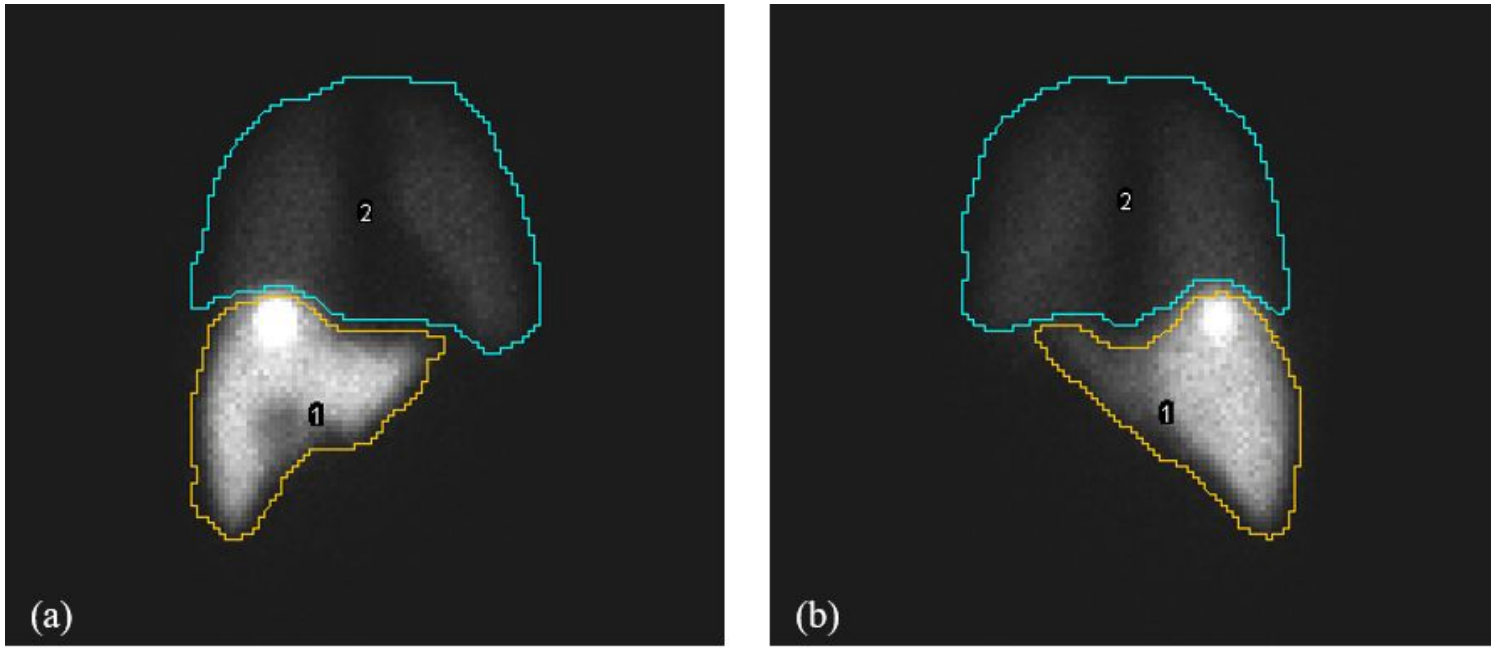


Figure 4

Liver (orange ROI) and lung segmentation (blue ROI) of planar images on (a) anterior and (b) posterior view.

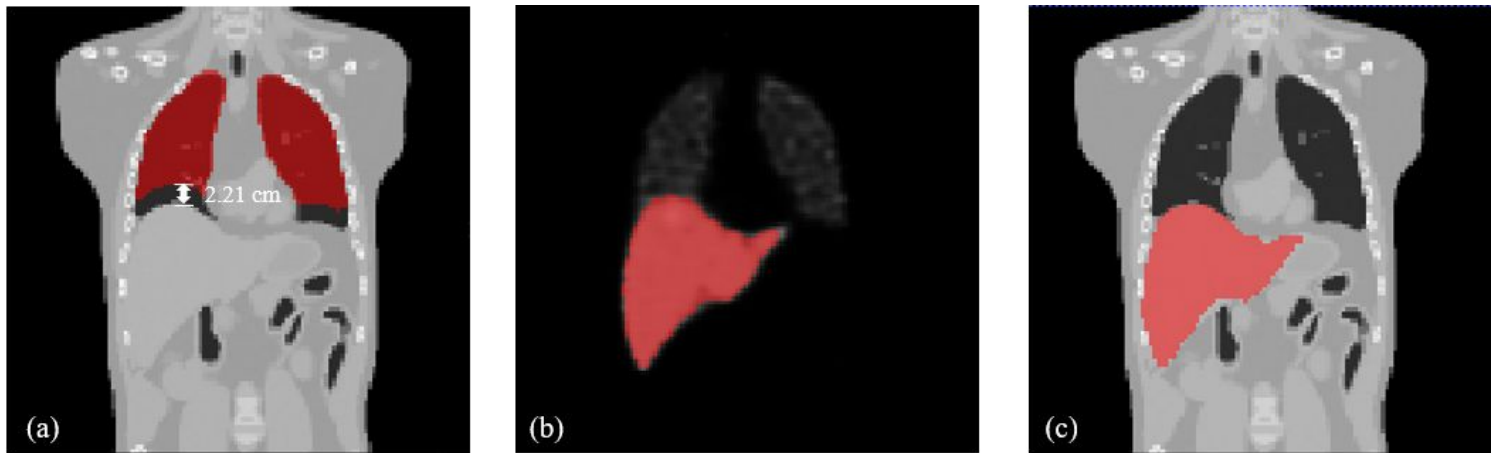


Figure 5

(a) Lung segmentation with 2.21 cm axial exclusion on HCT-MID. (b) Liver segmentation on SPECT image and on (c) HCT-MID for Phantom #1.

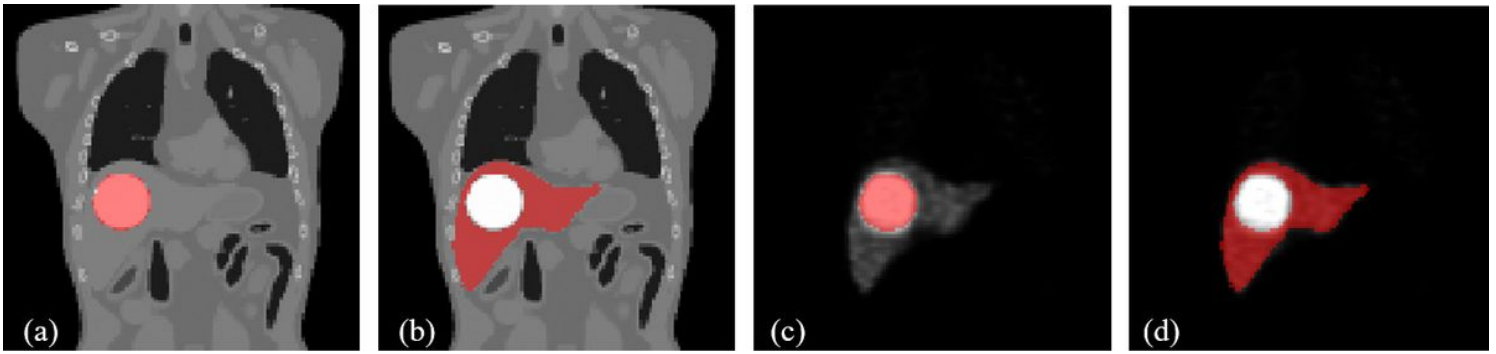


Figure 6

(a) Tumor and (b) NL segmentation on contrast HCT-MID. Corresponding VOIs were then mapped to segment the (c) tumor and (d) NL on SPECT images for Phantom #2.

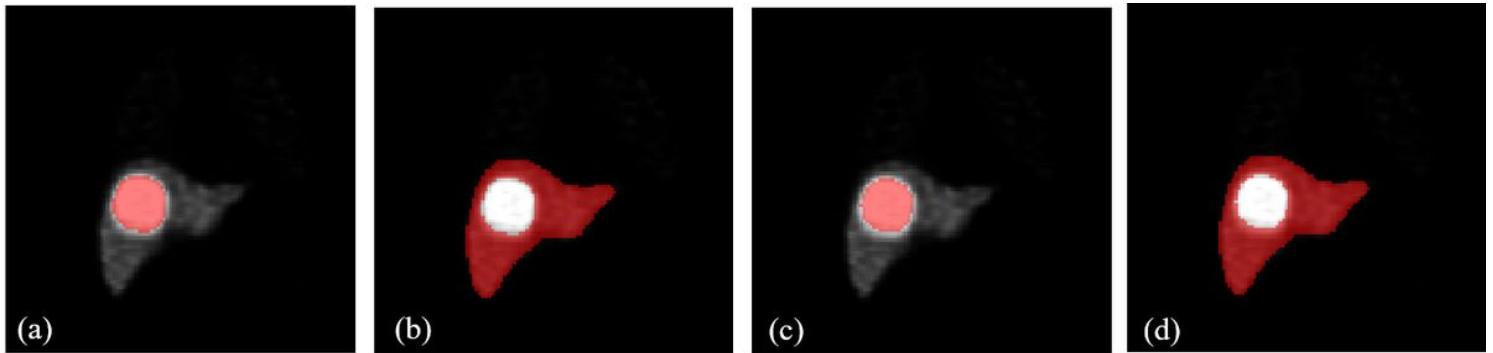


Figure 7

(a) Tumor segmented from 40% of maximum intensity and (b) corresponding NL VOI. (c) Tumor segmented from 50% of maximum intensity and (d) corresponding NL VOI on SPECT images for Phantom #2.

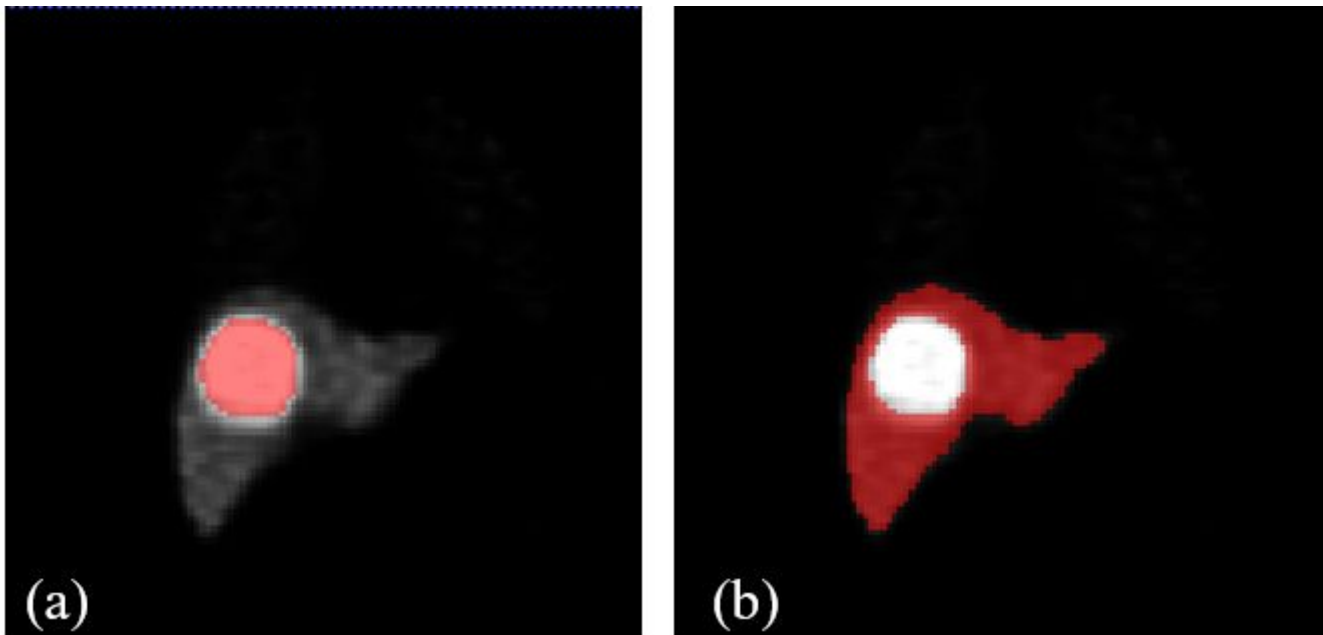


Figure 8

(a) Tumor and (b) NL VOIs on SPECT images such that their volumes equal to the volumes of corresponding VOIs from contrast HCT-EX for Phantom #2.

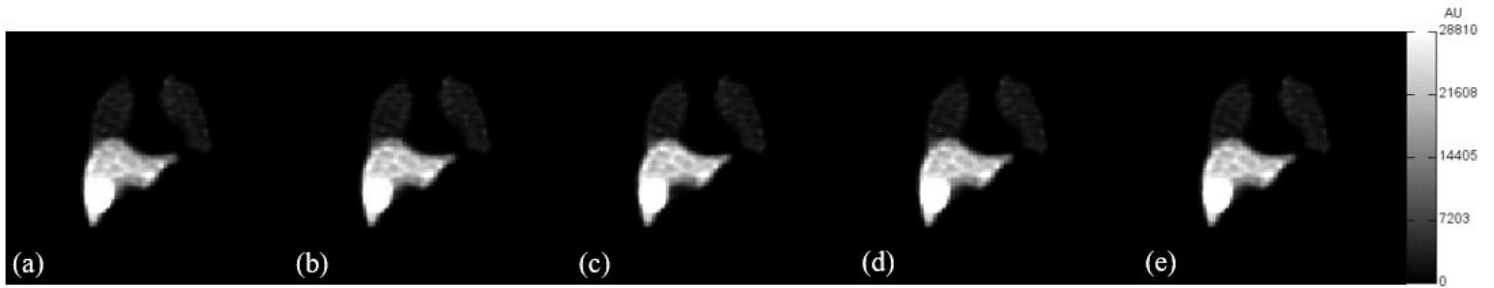


Figure 9

Reconstructed images of Phantom #9 with 20% LSF using (a) HCT-IN, (b) HCT-MID, (c) HCT-EX, (d) CACT and (e) IACT for AC. AU: Arbitrary unit.

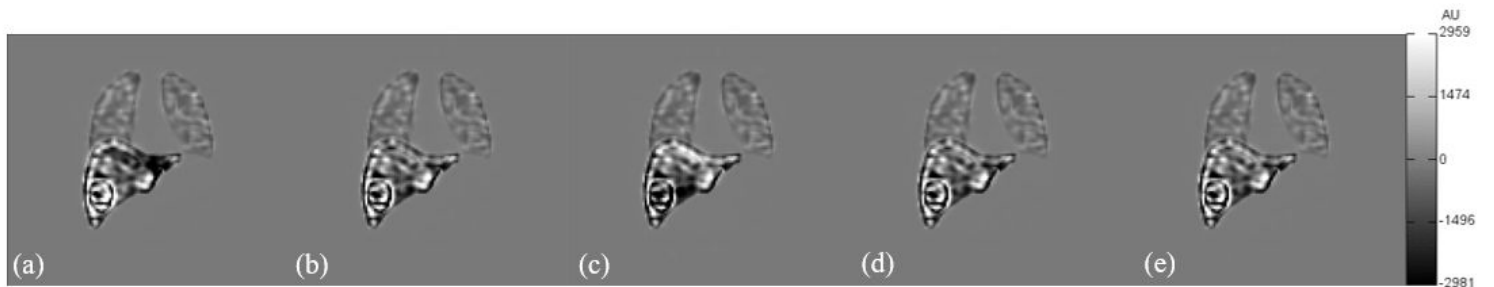


Figure 10

The difference images between reconstructed images of Phantom #9 with 20% LSF using (a) HCT-IN, (b) HCT-MID, (c) HCT-EX, (d) CACT and (e) IACT for AC and the true activity map. AU: Arbitrary unit.

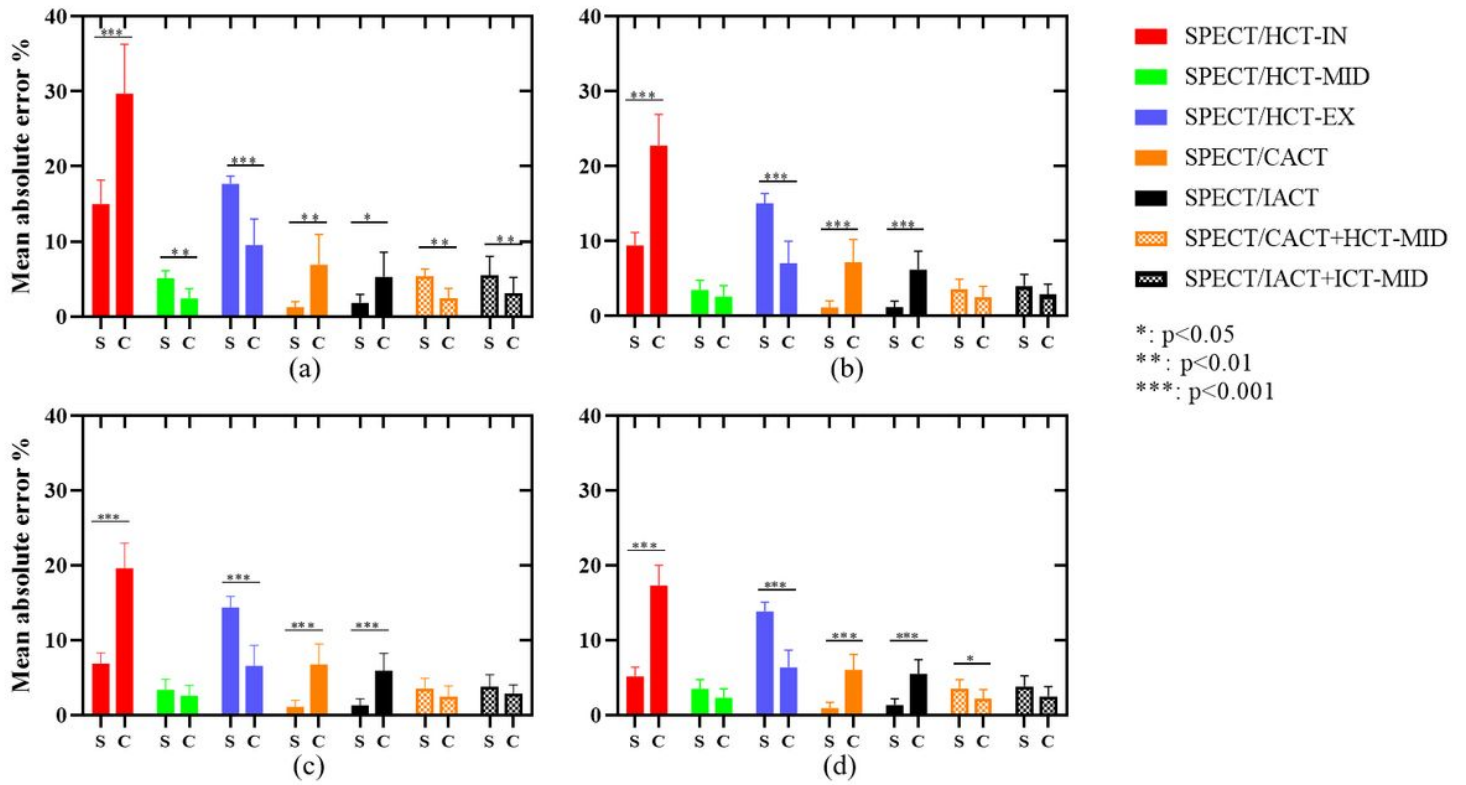


Figure 11

The mean absolute errors of LSF estimation for different CT protocols using SPECT- and CT-based segmentation methods to segment liver for a LSF of (a) 5%, (b) 10%, (c) 15% and (d) 20%, respectively. S: SPECT-based segmentation, C: CT-based segmentation.

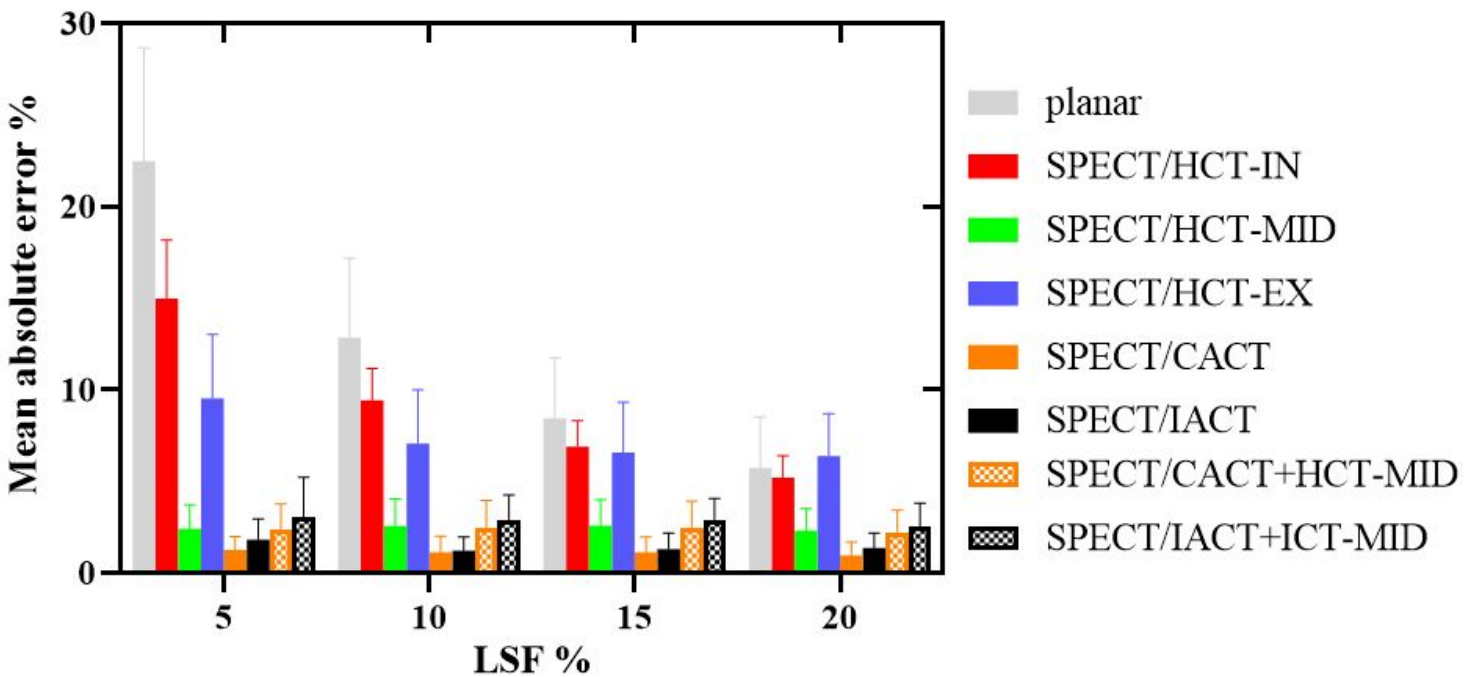


Figure 12

The mean absolute errors of LSF estimation from SPECT images with different CT protocols for AC and VOI segmentation.

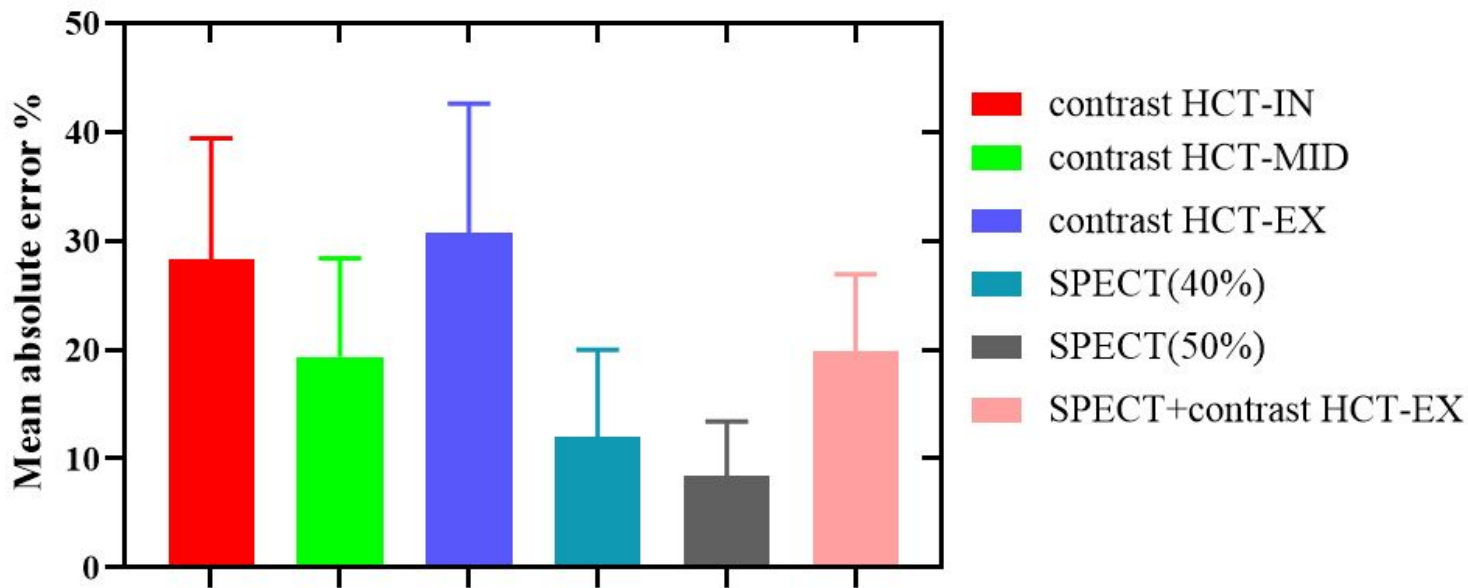


Figure 13

The mean absolute errors of TNR estimation for different tumor and NL segmentation methods for a LSF of 5%.

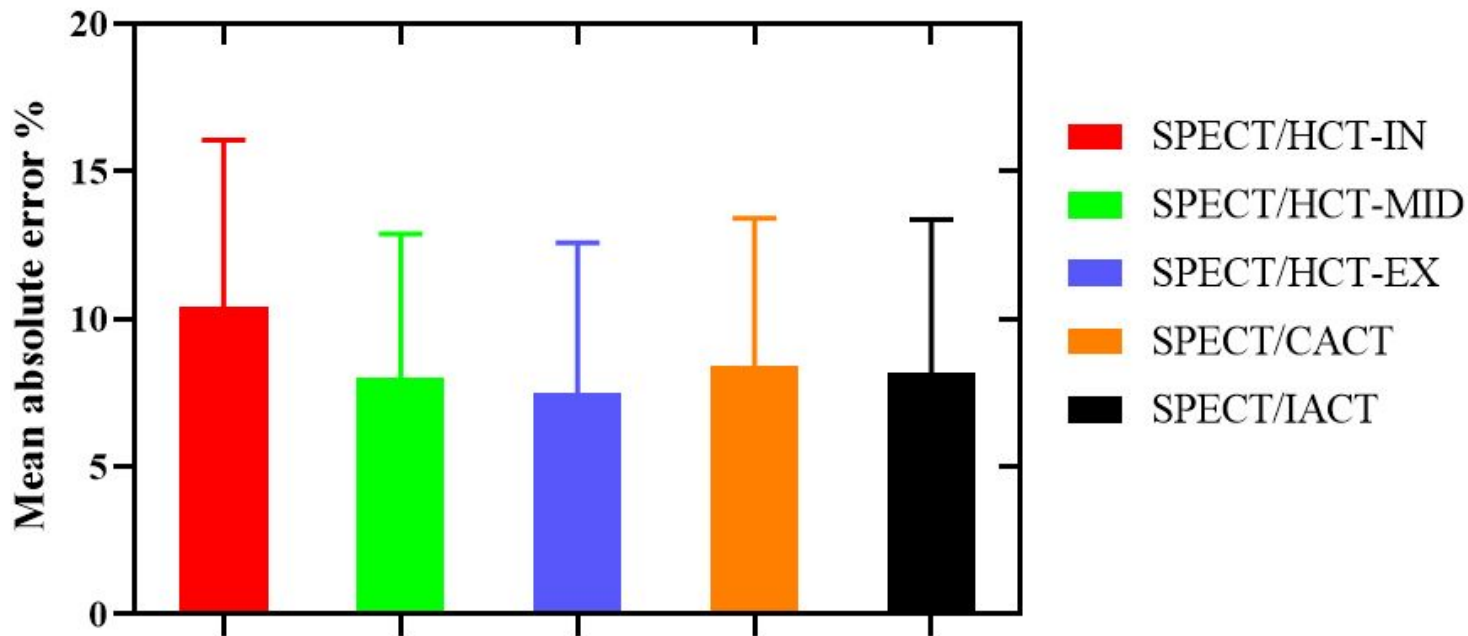


Figure 14

The mean absolute errors of TNR estimation from SPECT images with different AC protocols using SPECT(50%) segmentation method for a LSF of 5%.

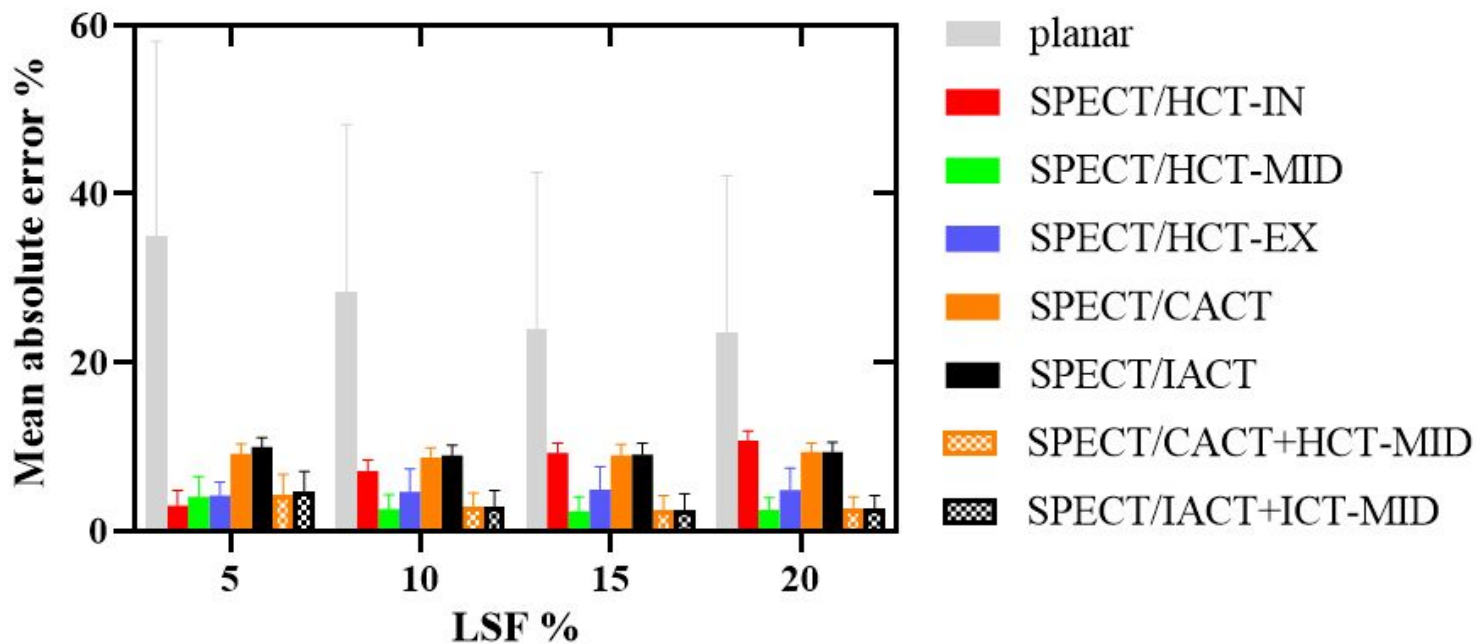


Figure 15

The mean absolute errors of lung absorbed dose estimation for 10 phantoms.

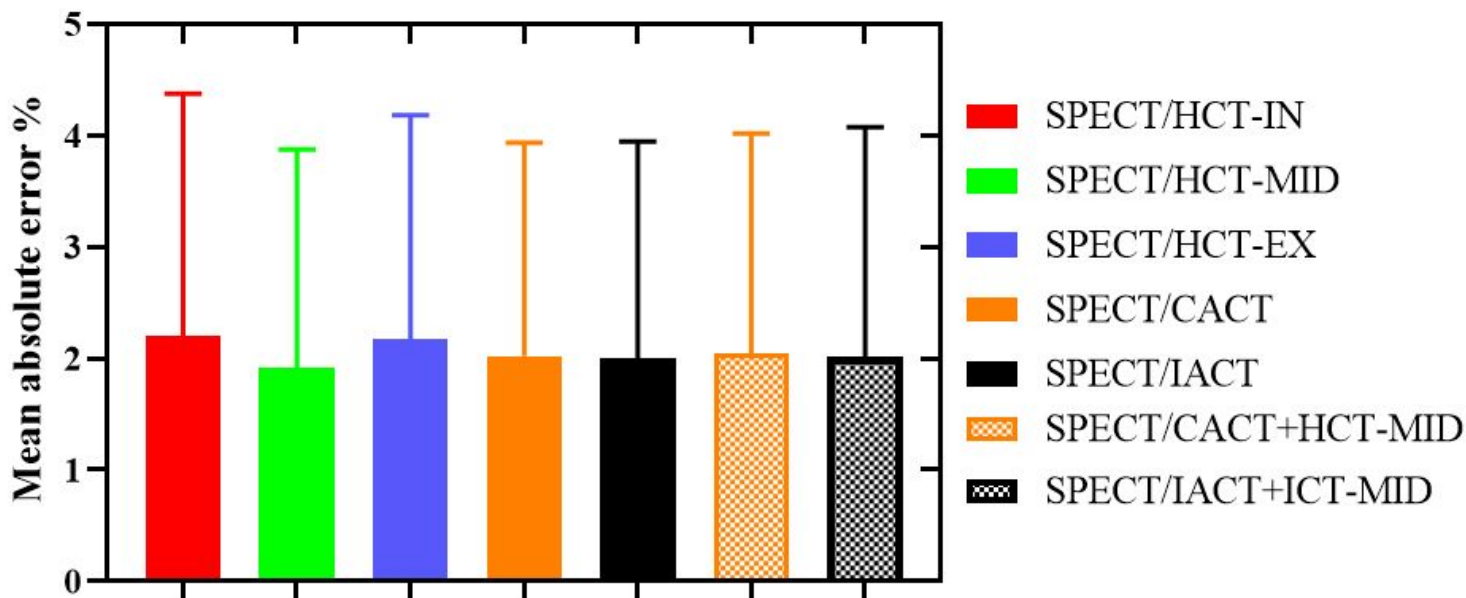


Figure 16

The mean absolute errors of NL absorbed dose estimation for 10 phantoms with LSF of 5%.

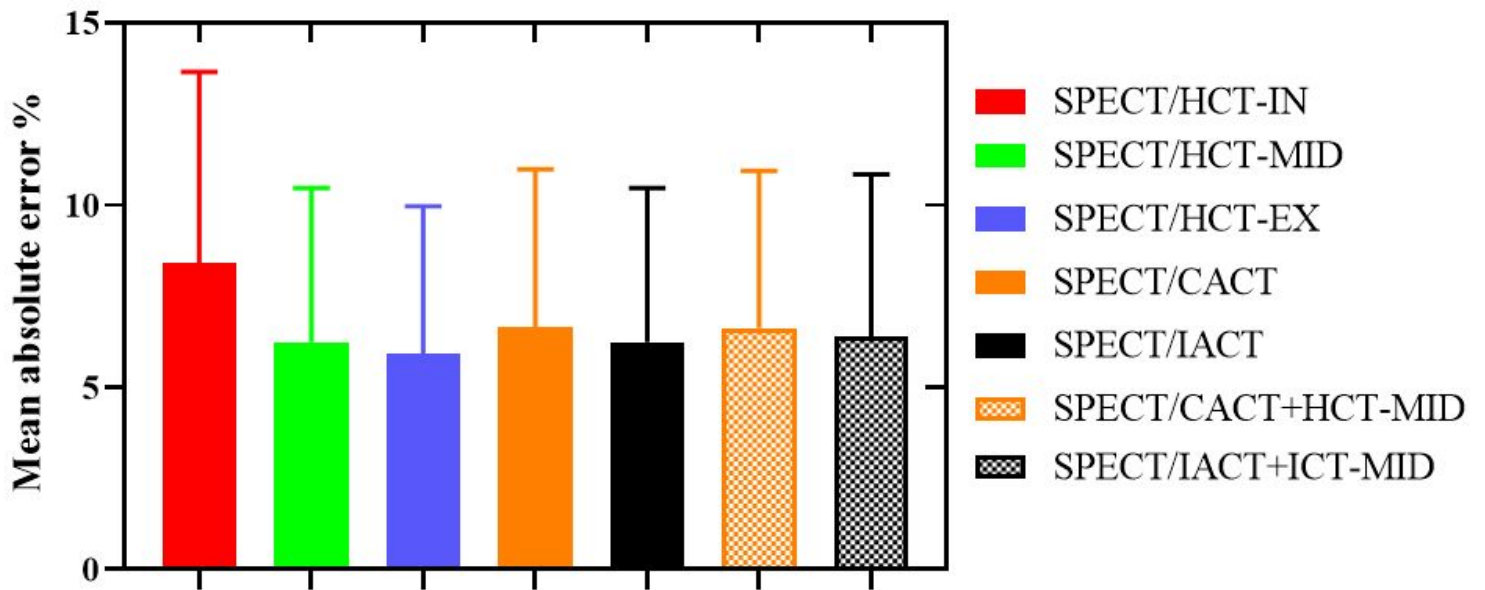


Figure 17

The mean absolute errors of tumor absorbed dose estimation for 10 phantoms with LSF of 5%.

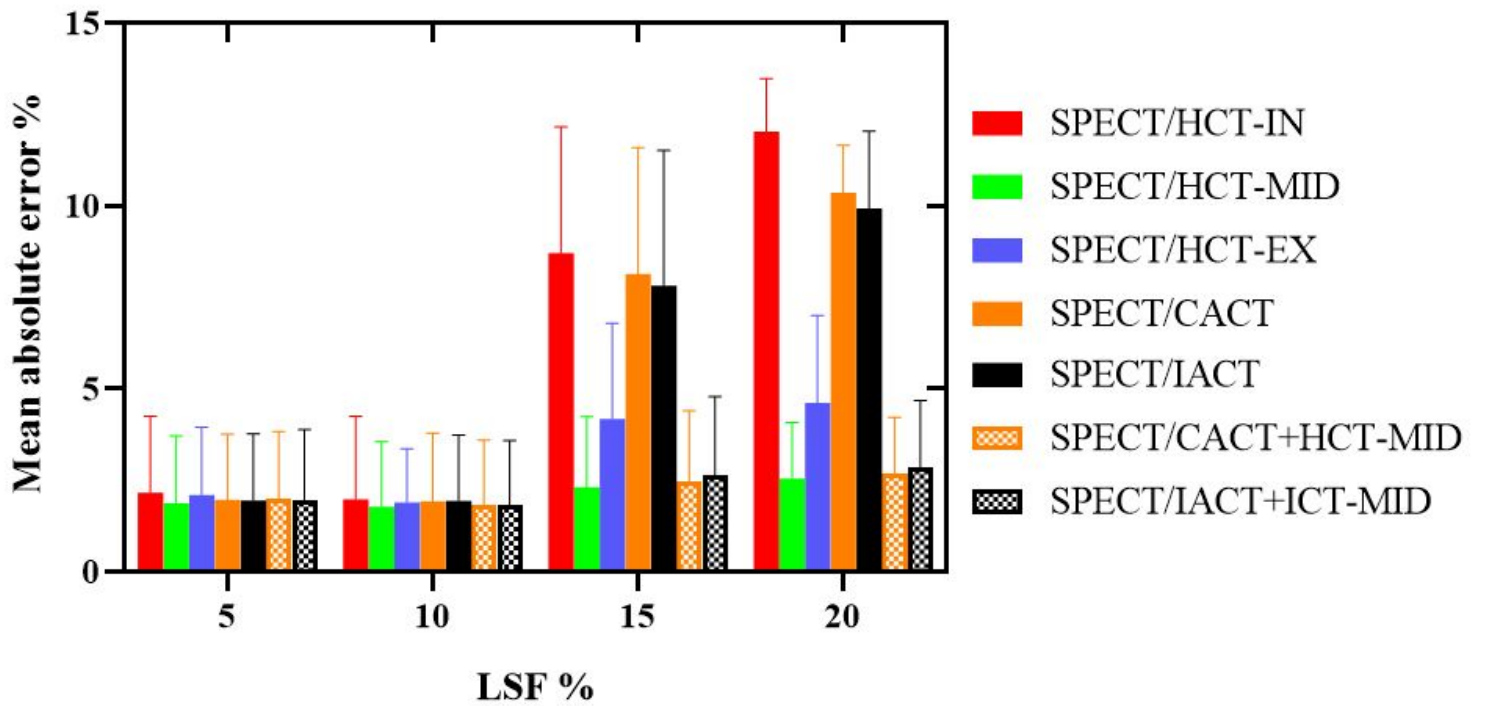


Figure 18

The mean absolute errors of IA estimation from 10 phantoms.